

Optimal Experiment Design for Magnetic Resonance Fingerprinting: Cramér-Rao Bound Meets Spin Dynamics

Bo Zhao, *Member, IEEE*, Justin P. Haldar, *Senior Member, IEEE*, Congyu Liao, Dan Ma, Mark A. Griswold, Kawin Setsompop, and Lawrence L. Wald, *Member, IEEE*

Abstract—Magnetic resonance (MR) fingerprinting is a new quantitative imaging paradigm, which simultaneously acquires multiple MR tissue parameter maps in a single experiment. In this work, we present a novel estimation-theoretic framework to perform optimal experiment design for MR fingerprinting. Specifically, we describe a discrete-time dynamic system to model spin dynamics. We then derive the estimation-theoretic bound, i.e., Cramér-Rao bound (CRB), to characterize the signal-to-noise ratio (SNR) efficiency of an MR fingerprinting experiment. We further formulate an optimal experiment design problem, which selects a sequence of acquisition parameters to encode MR tissue parameters with the maximal SNR efficiency, while respecting the physical constraints and other constraints from image decoding/reconstruction. We evaluate the performance of the proposed approach with numerical simulations and phantom experiments. We show representative results to demonstrate that the optimized experiments substantially reduce data acquisition time and/or improve parameter estimation accuracy. For example, with the optimized experiments, we are able to achieve about a factor of two improvement in the accuracy of T_2 maps, while keeping similar or slightly better accuracy of T_1 maps. Finally, as a remarkable observation, we find that the sequence of the optimized acquisition parameters appears to be highly structured rather than randomly/pseudo-randomly varying as prescribed in the conventional MR fingerprinting experiments.

Index Terms—Optimal experiment design, Cramér-Rao bound, spin dynamics, dynamic system, statistical inference, quantitative magnetic resonance imaging.

This work was partially supported by the National Institute of Health under Grant No. NIH-R01-EB017219 and NIH-R01-EB017337, and the National Science Foundation under Grant No. NSF-CCF-135063. B. Zhao was also supported by a Ruth L. Kirschstein National Research Service Award Postdoctoral Fellowship from the National Institute of Health under Grant No. NIH-F32-EB024381.

B. Zhao is with the Athinoula A. Martinos Center for Biomedical Imaging, Massachusetts General Hospital, Charlestown, MA 02129 USA, and also with the Department of Radiology, Harvard Medical School, Boston, MA 02115 USA (email: bzhao4@mgh.harvard.edu).

J. P. Haldar is with the Signal and Image Processing Institute and Ming Hsieh Department of Electrical Engineering, University of Southern California, Los Angeles, CA 90089 USA.

C. Liao is with the Athinoula A. Martinos Center for Biomedical Imaging, Massachusetts General Hospital, Charlestown, MA 02129 USA, and also with the Department of Biomedical Engineering, Zhejiang University, Hangzhou, Zhejiang Province 310027 China.

D. Ma and M. A. Griswold are with the Department of Radiology, Case Western Reserve University, Cleveland, OH 44106 USA.

K. Setsompop and L. L. Wald are with the Athinoula A. Martinos Center for Biomedical Imaging, Massachusetts General Hospital, Charlestown, MA 02129 USA, and also with the Department of Radiology, Harvard Medical School, Boston, MA, 02115 USA, and also with the Harvard-MIT Division of Health Sciences and Technology, Massachusetts Institute of Technology, Cambridge, MA 02139 USA (email: wald@nmr.mgh.harvard.edu).

I. INTRODUCTION

MAGNETIC resonance (MR) fingerprinting is a novel quantitative magnetic resonance imaging (MRI) framework [1]. It enables simultaneous quantification of multiple MR tissue parameter (e.g., T_1 , T_2 , and spin density) in a single imaging experiment with an ultrafast speed. Comparing to conventional MR relaxometry techniques (e.g., [2]–[6]), the original proof-of-principle MR fingerprinting implementation features with several key innovations in its encoding and decoding processes [1]. Specifically, in terms of encoding, it applies a series of time-varying, random or quasi-random data acquisition parameters (e.g., flip angles and repetition times) to probe the spin system, which generates unique transient-state signal evolutions, or fingerprints, for different MR tissue parameters; it further applies incoherent spatial encoding (e.g., variable density spiral acquisition) to collect k-space data. In terms of decoding, it performs a simple gridding reconstruction, and a dictionary-based pattern matching to obtain MR tissue parameter maps of interest.

Despite the revolutionary concept, some fundamental questions still remain unclear about the mechanism of MR fingerprinting. For example, from a theoretical perspective, the optimality of the encoding and decoding processes for MR fingerprinting have not been justified in [1]. While a recent work has performed a theoretical analysis of the MR fingerprinting problem from a low-dimensional manifold recovery viewpoint [7], this analysis is asymptotic and probabilistic in nature, and does not provide results that could be used to ensure the quality or guide the design of finite-duration MR fingerprinting experiments.

From a practical perspective, while existing MR fingerprinting methods work well in some scenarios, there are other important scenarios where the performance of these methods can be much worse. For example, the accuracy of T_2 maps from MR fingerprinting often depends critically on the length of data acquisition, and is much worse than the accuracy of T_1 maps as the acquisition length becomes short [8]–[12]. In these settings, it would be highly desirable to either improve parameter mapping quality without increasing experiment duration or reduce experiment duration without sacrificing parameter map quality. A general approach that can be used to achieve higher encoding efficiency and/or decoding accuracy would represent a major step forward for MR fingerprinting technology. It would improve existing applications and enable a range of

important new ones that were previously impractical due to unrealizable speed/quality requirements.

Recently, we introduced a novel statistical imaging framework for MR fingerprinting [8], [9]. On the decoding side, we proposed a maximum likelihood (ML) reconstruction approach, which directly reconstructs MR tissue parameter maps from highly-undersampled, noisy k -space data. Moreover, we showed analytically that the conventional reconstruction approach in [1] is sub-optimal from a statistical estimation perspective [8], [9]. The use of ML reconstruction has dramatically improved the estimation accuracy and/or reduced acquisition time. Apart from the quality of image decoding schemes, the performance of MR fingerprinting inherently depends on the quality of the available data. This motivates us to explore the optimization of MR fingerprinting on the encoding side, which naturally falls into the domain of experiment design in the statistical imaging framework.

In this paper, we address the optimal experiment design problem for MR fingerprinting. Our goal is to encode MR tissue parameters into the most informative measurements in the presence of noise. Specifically, we first model spin dynamics with a discrete-time dynamic system. We then calculate the estimation-theoretic bound, i.e., the Cramér-Rao bound (CRB) [13], as a measure of the signal-to-noise (SNR) efficiency for MR fingerprinting experiments. We further utilize this bound to formulate an optimal experiment design problem to choose MR fingerprinting acquisition parameters for the maximum SNR efficiency, while respecting both physical constraints and other constraints from image decoding. We show representative results from numerical simulations and phantom experiments to illustrate the performance of the optimized experiments. As a remarkable observation, we find that the sequence of optimized acquisition parameters appears to be highly structured rather than randomly/pseudo-randomly varying as used in the existing MR fingerprinting experiments (e.g., [1], [14]–[17]).

A preliminary account of this work was presented in our early conference papers [18], [19], which, to the best of our knowledge, first introduced the estimation-theoretic bound for MR fingerprinting experiment design. Recently, similar problems have also been investigated by other researchers. For example, Assländer et al. applied our approach to a new MR fingerprinting imaging sequence [15] under the polar coordinates of the Bloch equation [20]. Maidens et al. provided an optimal control interpretation of the experiment design problem, for which they developed a dynamic programming based algorithm [21]. However, due to the curse of dimensionality for dynamic programming [22], the feasibility of their approach was only demonstrated in a highly simplified scenario. Besides the CRB-based approaches, the experiment design problem was also addressed from other perspectives. For example, Cohen et al. optimized MR fingerprinting acquisition parameters by maximizing the discrimination power between different tissue types [23].

It is worth mentioning that the CRB has been previously used in analyzing and designing imaging experiments for conventional MR relaxometry (e.g., [24]–[32]). However, different from these conventional techniques, MR fingerprinting is a

transient-state imaging approach, which encodes MR tissue parameters into spin dynamics. In this context, the CRB calculation can be more complex, which involves handling a dynamic system, rather than an analytical signal model as in conventional MR relaxometry [24]–[31], [33]. In this paper, we introduce an efficient way of calculating the CRB for the Bloch equation based dynamic system. In particular, we show that such calculation can be done by iterating a set of finite-difference equations with some given initializations.

For easy reference, we summarize here the key notations and symbols used in the paper. We use \mathbb{R} to denote the field of real numbers, and use \mathbb{R}^n and $\mathbb{R}^{m \times n}$ to respectively denote the space of real vectors of length n and the space of real $m \times n$ matrices. We use bold letters (e.g., \mathbf{x} or \mathbf{X}) to denote vectors or matrices. We respectively use \mathbf{X}^T , \mathbf{X}^{-1} , and $\text{tr}(\mathbf{X})$ to denote the transpose, inverse, and trace of \mathbf{X} . For a scalar-valued function $f : \mathbb{R}^N \rightarrow \mathbb{R}$ with the argument $\mathbf{x} \in \mathbb{R}^N$, we define its gradient, i.e., $\partial f / \partial \mathbf{x}$, as an $N \times 1$ vector with $[\partial f / \partial \mathbf{x}]_n = \partial f / \partial x_n$; for a vector-valued function $F : \mathbb{R}^N \rightarrow \mathbb{R}^M$ with the argument $\mathbf{x} \in \mathbb{R}^N$, we define its Jacobian matrix, i.e., $\partial F / \partial \mathbf{x}$, as an $M \times N$ matrix with $[\partial F / \partial \mathbf{x}]_{m,n} = \partial F_m / \partial x_n$; and for a matrix-valued function $\mathbf{F} : \mathbb{R} \rightarrow \mathbb{R}^{M \times N}$ with the argument $x \in \mathbb{R}$, we define its derivative an $M \times N$ matrix with $[\partial \mathbf{F} / \partial x]_{m,n} = \partial \mathbf{F}_{m,n} / \partial x$. For a random vector $\mathbf{x} \in \mathbb{R}^N$, we denote the expectation as $\mathbb{E}[\mathbf{x}] \in \mathbb{R}^N$, and the covariance matrix as $\text{Cov}(\mathbf{x}) = \mathbb{E}[(\mathbf{x} - \mathbb{E}(\mathbf{x}))(\mathbf{x} - \mathbb{E}(\mathbf{x}))^T] \in \mathbb{R}^{N \times N}$.

The rest of the paper is organized as follows. Section II presents the proposed approach in detail, which starts with a state-space model for spin dynamics, followed by the Cramér-Rao bound calculation and optimal design of MR fingerprinting experiments. Section III demonstrates the performance of the optimized MR fingerprinting experiments with numerical simulations and phantom experiments. Section IV discusses related issues and future work, followed by the concluding remarks in Section V.

II. PROPOSED APPROACH

A. Signal Model

There are a variety of MR fingerprinting imaging sequences that have recently been developed (e.g., [1], [14]–[17]). In this subsection, we start by describing a generic state-space model for spin dynamics that underlie all MR fingerprinting experiments. We then give an example by specializing this model to a representative MR fingerprinting imaging sequence.

1) *State-Space Model*: Spin dynamics are governed by the Bloch equation [34], which is a system of first-order ordinary differential equations. While magnetization evolves in continuous time, we are mainly interested in its values at a finite set of time points in MR fingerprinting experiments. For convenience, we consider a discrete-time signal model, which should completely capture the features of interest for spin dynamics in continuous time. Moreover, here we focus on the magnetization evolution with respect to a small sample of tissue (i.e., a voxel); other issues related to spatial encoding will be discussed later.

In the presence of magnetic field inhomogeneity (e.g., with the use of gradients), intravoxel spin dephasing occurs. To

account for this effect, we model multiple isochromats in an imaging voxel, each of which represents an ensemble of spins that have the same phase dispersions. Here we can use the isochromat-summation approach [35], [36] to approximate the magnetization evolution for the imaging voxel of interest. Specifically, we first divide the voxel of interest, i.e., Δ , into a set of sufficiently small, equal-sized subvoxels $\{\Delta_{\mathbf{r}}\}$, where $\Delta_{\mathbf{r}}$ is centered at \mathbf{r} and $\Delta_{\mathbf{r}} \subset \Delta$. Here we assume that there exists a single isochromat for each $\Delta_{\mathbf{r}}$. We then analyze the magnetization evolution for each $\Delta_{\mathbf{r}}$. Finally, we obtain the overall magnetization for Δ by summing up all the magnetizations associated with the constituent subvoxels. Note that the above approach is general enough, in that it encompasses the special case that there exists only a single isochromat for the entire imaging voxel, i.e., all the subvoxels have the same phase dispersions.

We start by describing the magnetization evolution for each isochromat. Let $\mathbf{M}_{\mathbf{r}}[n] \in \mathbb{R}^3$ denote the magnetization associated with the isochromat for $\Delta_{\mathbf{r}}$ at the end of the n th repetition time (immediately before the next signal excitation). Here we can describe the magnetization evolution by the following state equation:

$$\mathbf{M}_{\mathbf{r}}[n] = \mathbf{A}_{\mathbf{r}}(\mathbf{u}[n], \boldsymbol{\theta})\mathbf{M}_{\mathbf{r}}[n-1] + \mathbf{B}_{\mathbf{r}}(\mathbf{u}[n], \boldsymbol{\theta}), \quad (1)$$

for $n = 1, \dots, N$, where $\boldsymbol{\theta} \in \mathbb{R}^p$ contains the unknown parameters in an MR fingerprinting experiment, including the tissue-specific parameters (e.g., T_1 , T_2 , and spin density) and experiment-specific parameters (e.g., off-resonance frequency); $\mathbf{u}[n] \in \mathbb{R}^q$ contains the data acquisition parameters applied during the n th repetition time, including the flip angle α_n , the phase of the radio frequency (RF) pulse ϕ_n , the echo time TE_n , and the repetition time TR_n ; $\mathbf{A}_{\mathbf{r}}(\mathbf{u}[n], \boldsymbol{\theta}) \in \mathbb{R}^{3 \times 3}$ and $\mathbf{B}_{\mathbf{r}}(\mathbf{u}[n], \boldsymbol{\theta}) \in \mathbb{R}^{3 \times 1}$ respectively denote the system matrix and input matrix for the n th repetition time. Note that in (1), we implicitly assume that all the subvoxels share the same set of parameter $\boldsymbol{\theta}$. The initial condition for (1) is given by $\mathbf{M}_{\mathbf{r}}[0] = [0, 0, M_0(\mathbf{r})]^T$, where $M_0(\mathbf{r}) = M_0/N_v$ denotes the magnitude of the magnetization for $\Delta_{\mathbf{r}}$ at thermal equilibrium, M_0 denotes the magnitude of magnetization for the entire imaging voxel Δ , and N_v denotes the number of the subvoxels within Δ .

The magnetization is measured at each echo time in MR fingerprinting experiments, and the signal detected by the RF receiver coil is approximately proportional to the transverse component of the magnetization. Denoting $\mathbf{m}_{\mathbf{r}}[n] \in \mathbb{R}^2$ as the transverse magnetization associated with $\Delta_{\mathbf{r}}$ at the n th echo time, we have

$$\mathbf{m}_{\mathbf{r}}[n] = \mathbf{C}_{\mathbf{r}}(\mathbf{u}[n], \boldsymbol{\theta})\mathbf{M}_{\mathbf{r}}[n-1], \quad (2)$$

for $n = 1, \dots, N$, where $\mathbf{C}_{\mathbf{r}}(\mathbf{u}[n], \boldsymbol{\theta}) \in \mathbb{R}^{2 \times 3}$ denotes the output matrix. Summing up all the magnetizations for each $\Delta_{\mathbf{r}}$, we can obtain the overall transverse magnetization for Δ as follows:

$$\mathbf{m}[n] = \sum_{\mathbf{r}: \Delta_{\mathbf{r}} \subset \Delta} \mathbf{m}_{\mathbf{r}}[n]. \quad (3)$$

Putting together (2) and (3), we have

$$\mathbf{m}[n] = \sum_{\mathbf{r}: \Delta_{\mathbf{r}} \subset \Delta} \mathbf{C}_{\mathbf{r}}(\mathbf{u}[n], \boldsymbol{\theta})\mathbf{M}_{\mathbf{r}}[n-1]. \quad (4)$$

The equations (1) and (4) together form a state-space model, which can describe spin dynamics for various MR fingerprinting imaging sequences (e.g., [1], [14]–[17]). Note that this model is nonlinear and time-varying in nature.

2) *Example Sequence:* As an example, we specialize the above state-space model to a widely-used MR fingerprinting pulse sequence, i.e., inversion recovery fast imaging with steady-state precession (IR-FISP) sequence [16]. Note that this sequence is robust to off-resonance effects with the use of dephasing gradients. Here the unknown parameters $\boldsymbol{\theta} = [T_1, T_2, M_0]^T$,¹ and the acquisition parameters $\mathbf{u}[n] = [\alpha_n, \phi_n, TE_n, TR_n]^T$.

In the IR-FISP sequence, three physical processes drive magnetization evolutions: (1) RF excitation; (2) spin relaxation; and (3) spin dephasing. Due to the presence of dephasing gradients, intravoxel spin dephasing occurs. To account for this effect, we assume that there are multiple isochromats within an imaging voxel, and use the isochromat-summation approach to model magnetization evolutions. Specifically, under the Cartesian coordinates in the rotating frame [37],² we can form the system matrix $\mathbf{A}_{\mathbf{r}}$ as

$$\mathbf{A}_{\mathbf{r}}(\mathbf{u}[n], \boldsymbol{\theta}) = \mathbf{G}(\beta_{\mathbf{r}})\mathbf{R}(T_1, T_2, TR_n)\mathbf{Q}(\alpha_n, \phi_n), \quad (5)$$

where $\mathbf{Q}(\alpha_n, \phi_n) \in \mathbb{R}^{3 \times 3}$ models the RF excitation, i.e.,

$$\mathbf{Q}(\alpha_n, \phi_n) = \begin{bmatrix} \cos(\phi_n) & \sin(\phi_n) & 0 \\ -\sin(\phi_n) & \cos(\phi_n) & 0 \\ 0 & 0 & 1 \end{bmatrix} \begin{bmatrix} 1 & 0 & 0 \\ 0 & \cos(\alpha_n) & \sin(\alpha_n) \\ 0 & -\sin(\alpha_n) & \cos(\alpha_n) \end{bmatrix} \begin{bmatrix} \cos(\phi_n) & -\sin(\phi_n) & 0 \\ \sin(\phi_n) & \cos(\phi_n) & 0 \\ 0 & 0 & 1 \end{bmatrix};$$

$\mathbf{R}(T_1, T_2, t) \in \mathbb{R}^{3 \times 3}$ models the spin relaxation, i.e.,

$$\mathbf{R}(T_1, T_2, t) = \begin{bmatrix} e^{-t/T_2} & 0 & 0 \\ 0 & e^{-t/T_2} & 0 \\ 0 & 0 & e^{-t/T_1} \end{bmatrix};$$

and $\mathbf{G}(\beta_{\mathbf{r}}) \in \mathbb{R}^{3 \times 3}$ models the spin dephasing, i.e.,

$$\mathbf{G}(\beta_{\mathbf{r}}) = \begin{bmatrix} \cos(\beta_{\mathbf{r}}) & \sin(\beta_{\mathbf{r}}) & 0 \\ -\sin(\beta_{\mathbf{r}}) & \cos(\beta_{\mathbf{r}}) & 0 \\ 0 & 0 & 1 \end{bmatrix},$$

where $\beta_{\mathbf{r}}$ denotes the phase dispersion associated with the isochromat at $\Delta_{\mathbf{r}}$. Note that in the IR-FISP sequence, $\beta_{\mathbf{r}}$ is dominated by the impact of dephasing gradients, although there are various other factors (e.g., susceptibility or diffusion effect) that can also contribute to spin dephasing.

Moreover, we can form the input matrix $\mathbf{B}_{\mathbf{r}}$ as

$$\mathbf{B}_{\mathbf{r}}(\mathbf{u}[n], \boldsymbol{\theta}) = M_0(\mathbf{r})\mathbf{b}(T_1, TR_n), \quad (6)$$

where $\mathbf{b}(T_1, t) = [0 \ 0 \ 1 - e^{-t/T_1}]^T$. Note that $\mathbf{B}_{\mathbf{r}}(\mathbf{u}[n], \boldsymbol{\theta})$ models the recovery of the longitudinal magnetization.

¹Note that M_0 , i.e., the magnitude of magnetization at thermal equilibrium, is proportional to the spin density at Δ [37]. Here the scaling constant depends on the field strength, the temperature of the spin system, the gyromagnetic ratio, etc.

²Alternatively, the model can be described in other coordinate systems (e.g., the polar coordinates [20]); however, note that the Cramér-Rao bound does not change under any transform of the coordinate system for the Bloch equations.

Finally, we can form the output matrix \mathbf{C}_r as

$$\mathbf{C}_r(\mathbf{u}[n], \boldsymbol{\theta}) = \mathbf{P}\mathbf{R}(T_1, T_2, TE_n)\mathbf{Q}(\alpha_n, \phi_n), \quad (7)$$

where $\mathbf{P} \in \mathbb{R}^{2 \times 3}$ is the projection matrix that extracts the transverse magnetization, i.e.,

$$\mathbf{P} = \begin{bmatrix} 1 & 0 & 0 \\ 0 & 1 & 0 \end{bmatrix},$$

and $\mathbf{R}(T_1, T_2, TE_n)$ and $\mathbf{Q}(\alpha_n, \phi_n)$ are defined in the same way as before. Note that $\mathbf{C}_r(\mathbf{u}[n], \boldsymbol{\theta})$ models the RF excitation as well as the spin relaxation. Since, within each repetition time, the dephasing gradient is placed after the echo time, this matrix does not account for the spin dephasing effect.

B. Cramér-Rao Bound

We proceed to describe the data model, with which we calculate the CRB and perform experiment design. Note that the spin dynamics described above are utilized to perform contrast encoding in MR fingerprinting experiments. Besides the contrast encoding, the data generating process also encompasses spatial encoding and noise contamination. In [8], [9], we described a data model for this data generating process. In principle, we can use it to calculate the CRB and perform experiment design. In practice, however, this can be computationally very expensive, due to the use of the nonCartesian Fourier transform in spatial encoding. Here we describe a practical approach, in which we ignore the spatial encoding, and use the following simplified data model:

$$\mathbf{s}[n] = \mathbf{m}[n] + \mathbf{z}[n], \quad (8)$$

for $n = 1, \dots, N$. Here $\mathbf{s}[n] \in \mathbb{R}^2$ is a vector that contains the magnetizations collected at the n th echo time, and $\{\mathbf{z}[n]\}_{n=1}^N$ denotes independent, identically distributed Gaussian noise with $\mathbf{z}[n] \sim N(\mathbf{0}, \sigma^2 \mathbf{I})$. Note that (8) corresponds to the data model for a single voxel nuclear magnetic resonance (NMR) experiment. Alternatively, it can also be viewed as the data model for a fully-sampled imaging experiment,³ in which there is no ‘‘crosstalk’’ between magnetization evolutions at different voxels. Despite such simplification, we will demonstrate later that the experiment design with (8) can be very effective for highly-undersampled MR fingerprinting experiments.

Next, we derive the CRB with (8). From estimation theory, the CRB provides a lower bound on the covariance of any unbiased estimator under mild regularity conditions, and this bound can be asymptotically achieved by the ML estimator [13]. Mathematically, we can express the CRB in the following information inequality [13]:

$$\mathbb{E} \left\{ \left(\boldsymbol{\theta} - \hat{\boldsymbol{\theta}} \right) \left(\boldsymbol{\theta} - \hat{\boldsymbol{\theta}} \right)^T \right\} \geq \mathbf{V}(\boldsymbol{\theta}) = \mathbf{I}^{-1}(\boldsymbol{\theta}), \quad (9)$$

for any unbiased estimator $\hat{\boldsymbol{\theta}}$, where $\mathbf{I}(\boldsymbol{\theta}) \in \mathbb{C}^{p \times p}$ denotes the Fisher information matrix (FIM) defined as [13]:

$$\mathbf{I}(\boldsymbol{\theta}) = \mathbb{E} \left[\left(\frac{\partial \ln p(\{\mathbf{s}[n]\}; \boldsymbol{\theta})}{\partial \boldsymbol{\theta}} \right) \left(\frac{\partial \ln p(\{\mathbf{s}[n]\}; \boldsymbol{\theta})}{\partial \boldsymbol{\theta}} \right)^T \right],$$

³More precisely, this is equivalent to a single-channel Nyquist-sampled Cartesian Fourier acquisition with a discrete Fourier transform based image reconstruction.

$\mathbf{V}(\boldsymbol{\theta}) \in \mathbb{C}^{p \times p}$ denotes the CRB matrix, and $\ln p(\mathbf{x}; \boldsymbol{\theta})$ denotes the log-likelihood function of the observation \mathbf{x} parameterized by $\boldsymbol{\theta}$. In (9), the matrix inequality $\mathbf{A} \geq \mathbf{B}$ means that $\mathbf{A} - \mathbf{B}$ is a positive semidefinite matrix. Here note that both the CRB and FIM depend on the underlying tissue parameter $\boldsymbol{\theta}$, given that the data model (8) is a nonlinear with respect to $\boldsymbol{\theta}$. Moreover, we can obtain the bound on the variance of individual tissue parameter estimate by extracting the corresponding diagonal entry of the CRB matrix, i.e.,

$$\text{Var}(\hat{\boldsymbol{\theta}}_i) \geq [\mathbf{V}(\boldsymbol{\theta})]_{i,i}. \quad (10)$$

To calculate the CRB in (9), we need to compute the FIM $\mathbf{I}(\boldsymbol{\theta})$. First, noting that $\mathbf{I}(\boldsymbol{\theta})$ is additive for the independent measurements $\{\mathbf{s}[n]\}_{n=1}^N$, we have

$$\mathbf{I}(\boldsymbol{\theta}) = \sum_{n=1}^N \mathbf{I}_n(\boldsymbol{\theta}), \quad (11)$$

where $\mathbf{I}_n(\boldsymbol{\theta})$ is the FIM associated with $\mathbf{s}[n]$, i.e.,

$$\mathbf{I}_n(\boldsymbol{\theta}) = \mathbb{E} \left[\left(\frac{\partial \ln p(\mathbf{s}[n]; \boldsymbol{\theta})}{\partial \boldsymbol{\theta}} \right) \left(\frac{\partial \ln p(\mathbf{s}[n]; \boldsymbol{\theta})}{\partial \boldsymbol{\theta}} \right)^T \right].$$

Second, for the Gaussian data model in (8), the FIM has the particularly simple form, which can be written as follows [13]:

$$\mathbf{I}_n(\boldsymbol{\theta}) = \frac{1}{\sigma^2} \mathbf{J}_n^T(\boldsymbol{\theta}) \mathbf{J}_n(\boldsymbol{\theta}), \quad (12)$$

where $\mathbf{J}_n(\boldsymbol{\theta}) = \partial \mathbf{m}[n] / \partial \boldsymbol{\theta} \in \mathbb{C}^{2 \times p}$ is the Jacobian matrix. Putting together (11) and (12), we have

$$\mathbf{I}(\boldsymbol{\theta}) = \frac{1}{\sigma^2} \sum_{n=1}^N \mathbf{J}_n^T(\boldsymbol{\theta}) \mathbf{J}_n(\boldsymbol{\theta}). \quad (13)$$

Finally, we describe the calculation of $\mathbf{J}_n(\boldsymbol{\theta})$ for (13). Given the state-space model in (1) and (4), such calculation is equivalent to solving a set of finite difference equations via recursion. More specifically, noting that

$$\mathbf{J}_n(\boldsymbol{\theta}) = \frac{\partial \mathbf{m}[n]}{\partial \boldsymbol{\theta}} = \begin{bmatrix} \frac{\partial}{\partial \theta_1} \mathbf{m}[n] & \cdots & \frac{\partial}{\partial \theta_p} \mathbf{m}[n] \end{bmatrix}, \quad (14)$$

we can compute $\partial \mathbf{m}[n] / \partial \theta_i$ for each entry of $\boldsymbol{\theta}$. This can be done as follows. First, we invoke the derivative with respect to θ_i on both sides of (4), which yields

$$\frac{\partial \mathbf{m}[n]}{\partial \theta_i} = \sum_{\mathbf{r}: \Delta_r \subset \Delta} \left\{ \frac{\partial \mathbf{C}_r(\mathbf{u}[n], \boldsymbol{\theta})}{\partial \theta_i} \mathbf{M}_r[n-1] + \mathbf{C}_r(\mathbf{u}[n], \boldsymbol{\theta}) \frac{\partial \mathbf{M}_r[n-1]}{\partial \theta_i} \right\}, \quad (15)$$

for $n = 1, \dots, N$. Then we invoke the derivative with respect to θ_i on both sides of (1), which yields

$$\begin{aligned} \frac{\partial \mathbf{M}_r[n]}{\partial \theta_i} &= \frac{\partial \mathbf{A}_r(\mathbf{u}[n], \boldsymbol{\theta})}{\partial \theta_i} \mathbf{M}_r[n-1] \\ &+ \mathbf{A}_r(\mathbf{u}[n], \boldsymbol{\theta}) \frac{\partial \mathbf{M}_r[n-1]}{\partial \theta_i} + \frac{\partial \mathbf{B}_r(\mathbf{u}[n], \boldsymbol{\theta})}{\partial \theta_i}. \end{aligned} \quad (16)$$

Now we can iterate the two finite difference equations (15) and (16) to calculate $\frac{\partial}{\partial \theta_i} \mathbf{m}[n]$. Note that the initial conditions are given by $\mathbf{M}_r[0] = [0, 0, M_0(\mathbf{r})]^T$ and $\partial \mathbf{M}_r[0] / \partial \theta_i =$

$[0, 0, \partial M_0(\mathbf{r})/\partial \theta_i]^T$. For the sake of concreteness, in the Appendix, we illustrate the above procedure with the example IR-FISP sequence.

C. Optimal Experiment Design

Given that the CRB provides a lower bound on the smallest possible variance for any unbiased estimator, we can use it to characterize the SNR efficiency. This helps understand the potential reliability of an MR fingerprinting experiment, or figure out how much acquisition time is necessary to achieve a certain level of quantitative accuracy. More importantly, we can use the CRB as a principled tool to optimize the encoding process for an MR fingerprinting experiment. Specifically, given a set of representative MR tissue parameters $\{\theta^{(l)}\}_{l=1}^L$, we can optimize data acquisition parameters of an MR fingerprinting experiment to maximize its SNR efficiency. Mathematically, we can formulate the following experiment design problem:

$$\begin{aligned} \min_{\mathbf{u}} \quad & \sum_{l=1}^L \Psi(\mathbf{V}(\theta^{(l)})) \\ \text{s.t.} \quad & \mathbf{u} \subset \mathcal{U}, \end{aligned} \quad (17)$$

where $\Psi(\cdot)$ denotes the design criterion, which is a scalar function of the CRB matrix; $\mathbf{u} = [\mathbf{u}[1], \dots, \mathbf{u}[N]] \in \mathbb{C}^{q \times N}$ denotes the acquisition parameters for an MR fingerprinting experiment with N time points; and $\mathcal{U} \subset \mathbb{C}^{q \times N}$ denotes the constraint set for feasible data acquisition parameters.

Here it is worth making a few remarks on (17). First, note that the above experiment design problem is essentially an multi-step decision-making problem [22], in which the acquisition parameter $\mathbf{u}[m]$ for the time point m impacts all subsequent spin dynamics (at the time points $n \geq m$). Second, in (17), we assume that the total number of time points, i.e., N , is given. In practice, N can be specified according to the desired experiment duration. Third, given that the CRB matrix depends on the underlying tissue parameter, we assume that, for a specific imaging application of interest (e.g., neuroimaging), we have the knowledge of the range of MR tissue parameter values prior to our experiment design. While it is desirable to design experiments that are universally optimal for all possible parameters of interest, this is not feasible in practice. As such, we select a few representative tissues as a practical compromise.

As an example, we specialize (17) to optimize MR fingerprinting experiments with the IR-FISP sequence. First, we specify the design criterion for $\Psi(\cdot)$. Note that there are various information criteria that can be used, including the A-optimality, D-optimality, and E-optimality criteria (see [38] for a comprehensive survey). Here we choose the A-optimality criterion [38], which minimizes the trace of the CRB matrix (i.e., the total variance of tissue parameter estimates). Further, we incorporate weightings into the design criterion, which is motivated by the following considerations: (1) the CRBs for different tissue parameters are often at very different scales; and (2) we may want to tailor a design to the parameters that are most relevant to specific applications of interest. Accordingly, we have $\Psi(\cdot) = \text{tr}(\mathbf{WV}(\theta))$, where \mathbf{W} is a

diagonal matrix whose diagonal entries contain weightings for different tissue parameters.

Second, we specify the data acquisition parameters $\mathbf{u} = [\mathbf{u}[1], \dots, \mathbf{u}[N]]$ for our experiment design. Note that the acquisition parameters for the IR-FISP sequence include the flip angles, RF pulse phases, echo times and repetition times. While we can optimize all of them in our experiment design, following the early work [14], we make a simpler treatment of the problem. Here we assume the flip angles and repetition times to be the design parameters, while fixing the RF pulse phases and echo times. Accordingly, we have $\mathbf{u}[n] = [\alpha_n, TR_n]^T$, for $n = 1, \dots, N$.

Lastly, we specify the constraint set \mathcal{U} for the acquisition parameters. Taking into account various physical considerations (e.g., specific absorption rate, and/or total acquisition time), we impose upper bounds and lower bounds for the acquisition parameters, i.e., $\alpha_n \in [\alpha_n^{\min}, \alpha_n^{\max}]$ and $TR_n \in [TR_n^{\min}, TR_n^{\max}]$, for $n = 1, \dots, N$. Accordingly, we can formulate the experiment design problem as follows:

$$\begin{aligned} \min_{\{\alpha_n, TR_n\}} \quad & \sum_{l=1}^L \text{tr}(\mathbf{WV}(\theta^{(l)})) \\ \text{s.t.} \quad & \alpha_n^{\min} \leq \alpha_n \leq \alpha_n^{\max}, \quad 1 \leq n \leq N, \\ & TR_n^{\min} \leq TR_n \leq TR_n^{\max}, \quad 1 \leq n \leq N. \end{aligned} \quad (18)$$

Besides the physical constraints, it is often useful to take into account other constraints from image decoding/reconstruction, especially when we deal with highly-undersampled MR fingerprinting experiments. While different reconstruction methods may use different strategies for image decoding (from highly-undersampled data), they often benefit from magnetization evolutions being smoothly varying.⁴ There are a number of ways to enforce this property. Here we incorporate an additional set of constraints into (18), which restricts the maximum flip angle variations between consecutive time points. As will be demonstrated later, such constraints are effective in promoting smooth magnetization evolutions, which yields better performance for image reconstruction with highly-undersampled data. Accordingly, we can formulate the experiment design problem as follows:

$$\begin{aligned} \min_{\{\alpha_n, TR_n\}_{n=1}^N} \quad & \sum_{l=1}^L \text{tr}(\mathbf{WV}(\theta^{(l)})) \\ \text{s.t.} \quad & \alpha_n^{\min} \leq \alpha_n \leq \alpha_n^{\max}, \quad 1 \leq n \leq N, \\ & TR_n^{\min} \leq TR_n \leq TR_n^{\max}, \quad 1 \leq n \leq N, \\ & |\alpha_{n+1} - \alpha_n| \leq \Delta \alpha_n^{\max}, \quad 1 \leq n \leq N-1. \end{aligned} \quad (19)$$

where $\Delta \alpha_n^{\max}$ specifies the maximum flip angle variations between α_n and α_{n+1} .

⁴For example, for the conventional reconstruction method [1] that utilizes direct pattern matching, smooth magnetization evolutions can be better differentiated from aliasing artifacts, leading to improved accuracy in dictionary matching. As another example, for the low-rank/subspace reconstruction method [12], smooth magnetization evolutions often result in a smaller low-rank approximation error given the same rank value. This in turn enables better reconstruction accuracy. Finally, for the statistical reconstruction methods [9], [39], which involve solving nonconvex optimization problems, an initialization from the improved conventional reconstruction or low-rank reconstruction method often leads to better performance.

The proposed formulations in (18) and (19) result in nonlinear and nonconvex optimization problems. A number of algorithms can be employed to solve these optimization problems, including nonlinear optimization methods [40] and stochastic optimization methods [41]. As an example, we use a state-of-the-art nonlinear programming method, i.e., sequential quadratic programming (SQP) [40], to seek local minima for (18) and (19). As with other nonlinear programming methods, the performance of the SQP algorithm is generally dependent on initialization. Here we initialize the algorithm with the acquisition parameters from the conventional MR fingerprinting experiment [14], with which the algorithm consistently yields good performance, although other initialization schemes (e.g., a multi-start strategy) may lead to better performance.

III. RESULTS

In this section, we show representative results from both numerical simulations and phantom experiments to illustrate the performance of the proposed method.

A. Simulations

1) *General Setup*: Here we consider a neuroimaging application for our simulations. Specifically, we created a numerical brain phantom to simulate single-channel MR fingerprinting experiments. We took the T_1 , T_2 , and M_0 maps from the Brainweb database [42] as our underlying ground truth, as shown in Fig. 1. We set the experimental field-of-view (FOV) as $300 \times 300 \text{ mm}^2$, and the matrix size as 256×256 . We simulated MR fingerprinting experiments with the IR-FISP sequence [14], which is robust to main magnetic field inhomogeneity. Moreover, for simplicity, we assumed that the transmit RF field was homogeneous in our simulations.

We performed Bloch simulations to generate contrast-weighted images for the IR-FISP sequence. Here we used the isochromat-summation approach [35], [36], with which we simulated magnetization evolutions for each voxel with 400 isochromats.⁵ Here we assumed that the phase dispersions of these isochromats, i.e., $\{\beta_r\}$, were uniformly distributed in $[-\pi, \pi]$. In Bloch simulations, we considered three different sets of acquisition parameters, respectively, from the conventional scheme [14], the optimized scheme with (18), as well as the optimized scheme with (19). In Fig. 2, we show the acquisition parameters from the conventional scheme with $N = 1000$, as well as the resulting magnetization evolutions for a white matter tissue and a grey matter tissue (as marked in Fig. 1 (a)). In the next subsection, we will describe the acquisition parameters from optimized experiments in detail. We generated k-space data from contrast-weighted images using the non-uniform Fourier transform [45]. In our simulations, we considered two setups of MR fingerprinting experiments:

- Fully-sampled experiment: we acquired fully-sampled Cartesian k-space data for each time point (or TR index), as in [46].

- Highly-undersampled experiment: we acquired highly-undersampled spiral k-space data at each time point, as in [14]. More specifically, we used the same spiral trajectory as [14], and acquired only one spiral interleaves for each time point (the fully-sampled data consist of 48 spiral interleaves).

We added complex white Gaussian noise to the measured data according to the pre-specified noise level σ^2 . Here we defined the signal-to-noise ratio as $\text{SNR} = 20 \log_{10}(s/\sigma)$, where s denotes the average value of M_0 in a region of white matter.

We performed the ML reconstruction [8], [9] for the above experiments. Note that for the fully-sampled experiments, the ML approach is equivalent to the direct Fourier reconstruction, followed by the dictionary-based pattern matching [47]. For the highly-undersampled experiments, we solved the reconstruction problem with the algorithm in [8], [9], for which we initialized with the gridding reconstruction. Here the dictionary used in the ML reconstruction was constructed based on the following parameter discretization scheme: the range of T_1 values was set as $[20, 3000] \text{ ms}$, in which we used an increment of 10 ms for $[20, 1500] \text{ ms}$ and an increment of 30 ms for $[1501, 3000] \text{ ms}$; the range of T_2 values was set as $[30, 500] \text{ ms}$, in which we used an increment of 1 ms for $[30, 200] \text{ ms}$ and an increment of 5 ms for $[201, 500] \text{ ms}$.

To assess the reconstruction accuracy, we used the following two metrics: (a) overall error, i.e., $\|I - \hat{I}\|_2 / \|I\|_2$, where I and \hat{I} respectively denote the true parameter map and reconstructed parameter map, and (b) voxelwise relative error, i.e., $|I_v - \hat{I}_v| / |I_v|$, where I_v and \hat{I}_v respectively denote the values of I and \hat{I} at the v th voxel.

2) *Experiment design with (18) and (19)*: Here we describe the detailed implementation of the proposed experiment designs for the neuroimaging application considered above. For convenience, we refer to the optimized schemes with (18) and (19) as Optimized-I and Optimized-II, respectively. In this work, we assumed that T_1 and T_2 were of primary interest, for which we manually chose the weighting matrix \mathbf{W} to ensure the good performance of our experiment design.⁶ Moreover, we chose three training tissues, i.e., $\theta^{(1)} = [700 \text{ ms}, 60 \text{ ms}, 0.6]$, $\theta^{(2)} = [850 \text{ ms}, 50 \text{ ms}, 0.6]$, and $\theta^{(3)} = [1100 \text{ ms}, 102 \text{ ms}, 0.6]$, for (18) and (19).⁷

We further specify the constraints for the acquisition parameters in (18) and (19). Here we set the maximum flip angle as

$$\alpha_n^{\max} = \begin{cases} 180^\circ, & \text{if } n = 1, \\ 60^\circ, & \text{if } 2 \leq n \leq N. \end{cases}$$

Note that this allows an 180° inversion pulse imposed at the beginning of imaging experiments. We set the minimum flip angle as $\alpha_n^{\min} = 10^\circ$ for $1 \leq n \leq N$. We respectively set the maximum and minimum repetition times as $TR_n^{\max} = 15 \text{ ms}$ and $TR_n^{\min} = 11 \text{ ms}$ for $1 \leq n \leq N$. Here, it is worth mentioning that the above constraints roughly match the range

⁶We used the same weighting matrix \mathbf{W} for both (18) and (19), which facilitates the subsequent comparison.

⁷Given that M_0 is a linear parameter for (8), the CRB of M_0 does not depend on the value of M_0 . Here we simply set the same M_0 value for the three training tissues.

⁵Note that the accuracy of this approach depends on the number of isochromats used for Bloch simulations [35], [36]. Here with a total number of 400 isochromats, we can obtain very good accuracy compared to the widely-used extended phase graph formalism [43], [44].

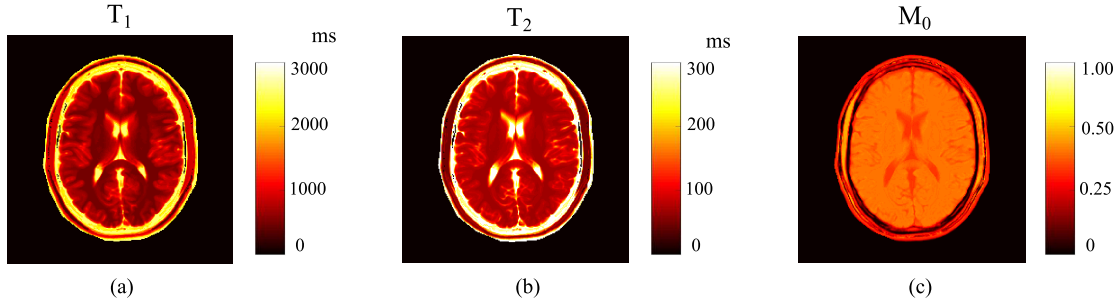


Fig. 1. Ground truth parameter maps for the brain phantom: (a) T_1 map, (b) T_2 map, and (c) M_0 map.

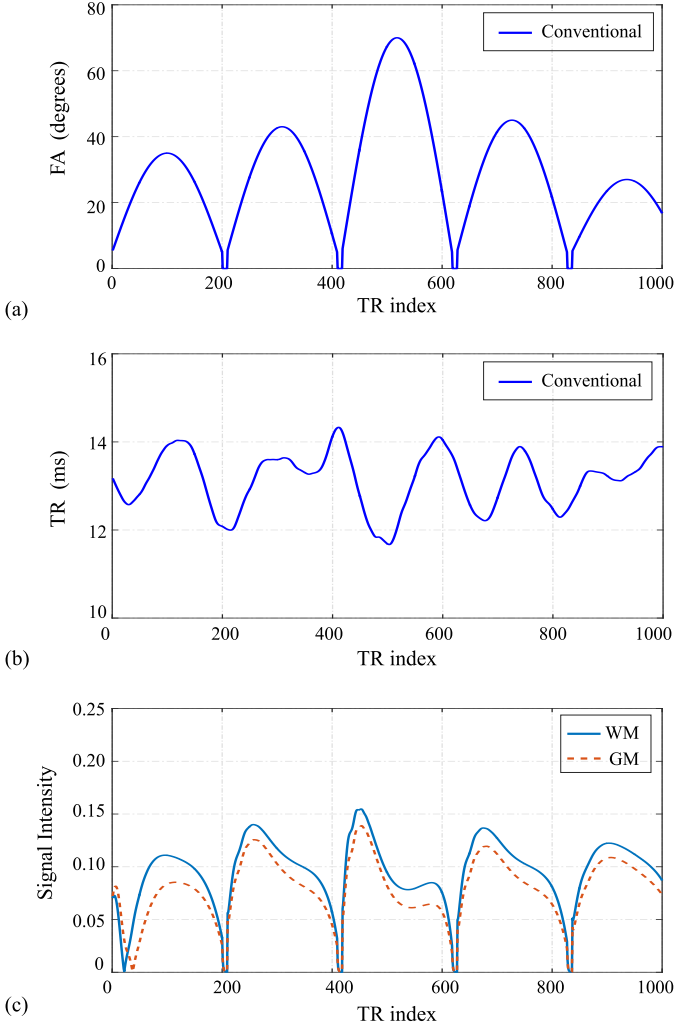


Fig. 2. Acquisition parameters for the conventional scheme with $N = 800$ as well as the resulting magnetization evolutions. (a) Flip angle train. (b) Repetition time train. (c) Magnetization evolutions for a white matter tissue and a gray matter tissue, as marked in Fig. 1 (a).

of the acquisition parameters in the conventional scheme. For (19), we have the additional constraints on the flip angle variations, which were set as

$$\Delta\alpha_n^{\max} = \begin{cases} +\infty, & \text{if } n = 1, \\ 1^\circ, & \text{if } 2 \leq n \leq N - 1. \end{cases}$$

Note that this constraint does not restrict the flip angle

variation between the inversion pulse and its subsequent RF pulse.

We applied the SQP algorithm to solve the optimization problems associated with (18) and (19). As mentioned before, we initialized the algorithm with the acquisition parameters from the conventional scheme. Regarding the stopping criterion, we terminated the algorithm, when the change of the solution was less than the pre-specified tolerance (i.e., $\epsilon = 1e^{-4}$) or the maximum iteration (i.e., $J_{\max} = 5 \times 10^4$) was reached. The runtime of the algorithm depends on the length of acquisition, i.e., N . For example, with $N = 400$, solving (18) and (19) respectively took about 290 min and 140 min on a Linux workstation with 24 Intel Xeon E5-2643, 3.40 GHz processors and 128 GB RAM running Matlab R2015b.

We optimized the acquisition parameters for every 100 time points, starting from $N = 300$ to $N = 800$. Fig. 3 shows the optimized acquisition parameters with $N = 400$ from Optimized-I and Optimized-II. As can be seen, the optimized acquisition parameters appear to be highly structured, which are remarkably different from the acquisition parameters from the conventional scheme. In particular, the optimized repetition times turn out to be binary (i.e., switching between TR_n^{\max} and TR_n^{\min}). Besides the above results, we also had similar observations for all other acquisition lengths. In the supplementary material, we show one more example, i.e., the optimized acquisition with $N = 600$. In Section IV, we will have more discussions on such behavior, and also point out its potential connection with optimal control theory.

Fig. 3 also shows the resulting magnetization evolutions from Optimized-I and Optimized-II. As can be seen, the magnetization evolutions from Optimized-I exhibit significant oscillation due to the dramatic change of acquisition parameters (within the first 100 time points). In contrast, by enforcing the additional constraints on the flip angle variations, the magnetization evolutions from Optimized-II appear to be much smoother (i.e., the oscillation behavior has been significantly suppressed). Later we will demonstrate that this is advantageous for image reconstruction from highly-undersampled data.

3) *Evaluation of CRB*: We evaluated the CRBs for the conventional scheme, Optimized-I, and Optimized-II. Note that the CRB is a lower bound on the variance (or equivalently the mean-square error) of an unbiased estimator. It provides a useful measure for the SNR properties of different imaging experiments from an estimation-theoretic perspective. Also,

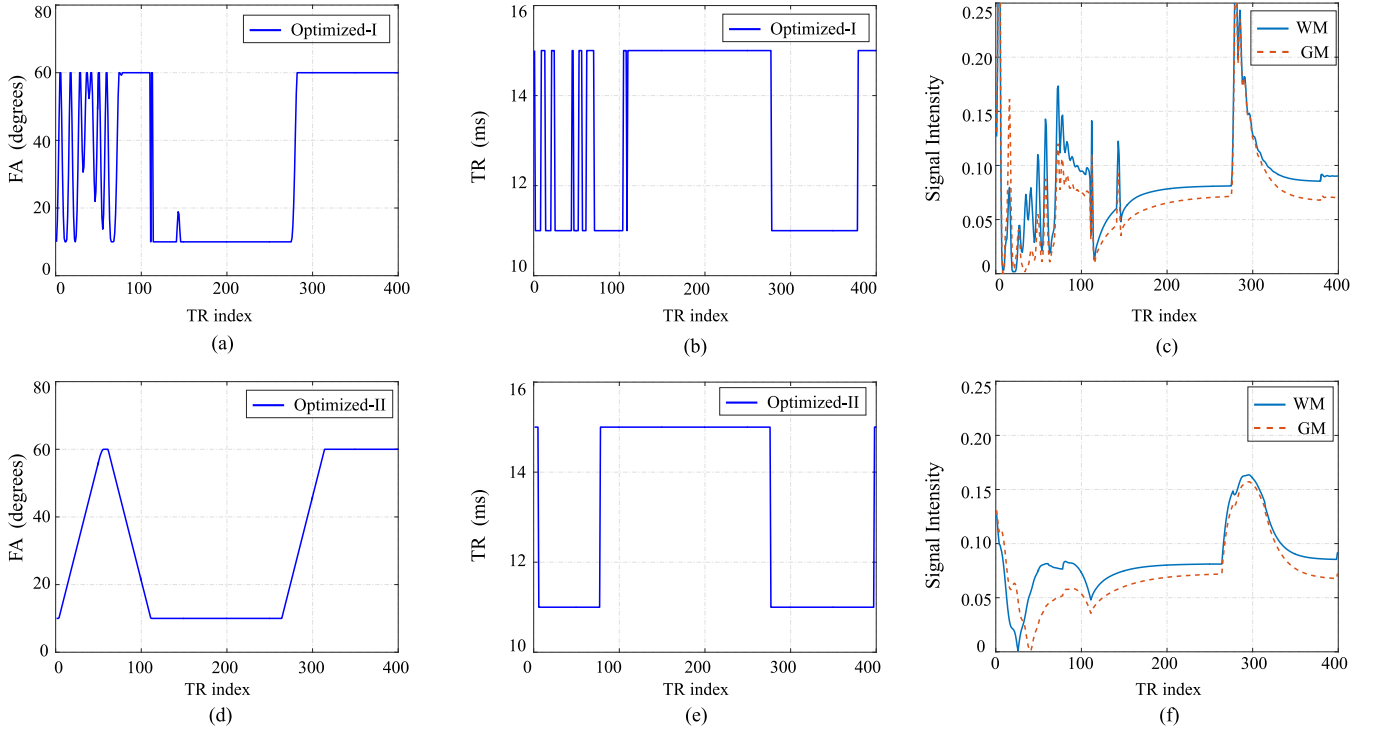


Fig. 3. Two optimized acquisition schemes with $N = 400$, and the resulting magnetization evolutions for the white matter tissue and the grey matter tissue marked in Fig. 1 (a). (a) Flip angle train for Optimized-I. (b) Repetition time train for Optimized-I. (c) Magnetization evolutions resulting from Optimized-I. (d) Flip angle train for Optimized-II. (e) Repetition time train for Optimized-II. (f) Magnetization evolutions resulting from Optimized-II. Note that with the additional constraints on the flip angle variations, the magnetization evolutions in Optimized-II appear to be much smoother.

note that our CRB calculation was for the data model (8), which exactly corresponds to the fully-sampled experiments considered here.

We calculated the CRBs associated with the conventional scheme, Optimized-I, and Optimized-II for different acquisition lengths at $\text{SNR} = 33$ dB. In order to show the CRBs for T_1 and T_2 at the same scale, we used the normalized CRB defined as $\text{nCRB}_i = \sqrt{\text{CRB}(\theta_i)}/\theta_i$. Fig. 4 shows the normalized CRBs associated with three acquisition schemes for the white matter tissue (marked in Fig. 1 (a)). As expected, for all three acquisition schemes, the nCRBs of T_1 and T_2 reduce, as the acquisition length becomes longer. However, note that the nCRBs for the conventional scheme and two optimized schemes exhibit very different behaviors. More specifically, for the conventional scheme, the nCRB for T_1 rapidly approaches its asymptotic limit, while attaining a good nCRB for T_2 requires significantly longer acquisition. Note that this is consistent with the previous observations in [8]–[12], and also suggests the sub-optimality of the conventional scheme from an estimation-theoretic perspective. In contrast, the nCRBs from Optimized-I and Optimized-II outperform the conventional scheme for both T_1 and T_2 over all the acquisition lengths. In particular, there is a substantial improvement for T_2 , as the acquisition length becomes short. Note that this can be highly desirable for achieving good accuracy for both T_1 and T_2 with a short acquisition time.

Here it is also worth pointing out that the nCRBs for Optimized-I are slightly better than those for Optimized-II. This is as expected, since, with a smaller set of constraints,

Optimized-I searches for a larger feasible space of acquisition parameters. Nonetheless, the difference between the two optimized schemes is quite small. In the supplementary material, we also show the CRB evaluation with respect to the gray matter tissue (marked in Fig. 1 (a)), from which we had very similar observations.

4) *Evaluation of fully-sampled experiments:* We considered the fully-sampled MR fingerprinting experiments as described in Section III (a). Specifically, we simulated the imaging experiments at $N = 400$ and $\text{SNR} = 33$ dB, using three different sets of acquisition parameters, i.e., the conventional acquisition scheme, Optimized-I, and Optimized-II. Fig. 5 shows the reconstructed T_1 and T_2 maps from the above experiments. As can be seen, the accuracy for both T_1 and T_2 maps improves with the two optimized acquisition schemes. In particular, the optimized schemes provide substantial improvement for the T_2 map. Moreover, the performance of Optimized-I is slightly better than that of Optimized-II for the fully-sampled experiments. Note that the above observations are consistent with the previous CRB calculation.

We further investigated the bias-variance property of the reconstructed parameter maps. Specifically, we performed Monte Carlo simulations of the fully-sampled MR fingerprinting experiments with 100 trials. We calculated the bias, variance, and mean square error of the reconstructed parameter maps. To compare these quantities at the same scale, we used the normalized bias, variance, and root-mean-square error defined as follows: (1) normalized bias:

$$\text{NBias}_v = \hat{\mathbb{E}} \left[\left\| \mathbf{I}_v - \hat{\mathbf{I}}_v \right\| \right] / \mathbf{I}_v,$$

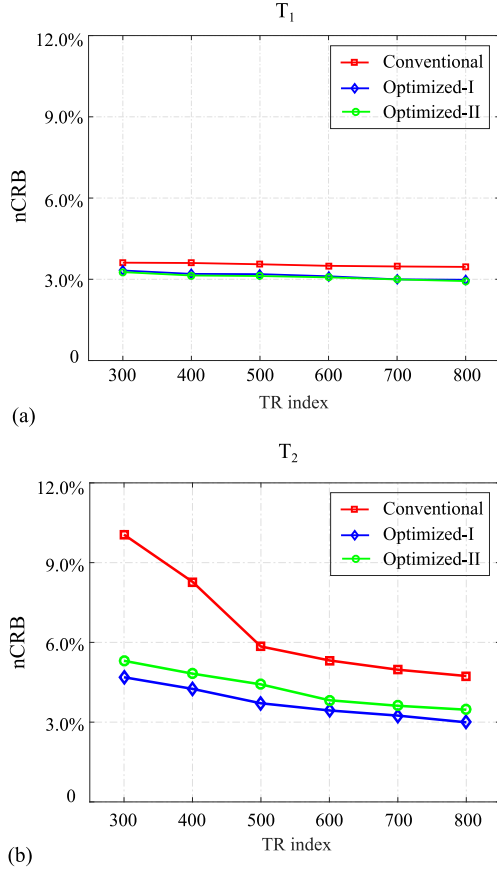


Fig. 4. Normalized CRB versus acquisition length for the white matter tissue associated with the conventional acquisition scheme and two optimized acquisition schemes. (a) Normalized CRBs for T_1 . (b) Normalized CRBs for T_2 .

(2) normalized variance:

$$\text{NVar}_v = \sqrt{\hat{\mathbb{E}} \left[\left| \mathbf{I}_v - \hat{\mathbf{E}}(\mathbf{I}_v) \right|^2 \right]} / \mathbf{I}_v,$$

and (3) normalized root-mean-square error:

$$\text{NRMSE}_v = \sqrt{\hat{\mathbb{E}} \left[\left| \mathbf{I}_v - \hat{\mathbf{I}}_v \right|^2 \right]} / \mathbf{I}_v,$$

where $\hat{\mathbb{E}}(\cdot)$ denotes the empirical mean evaluated for the MC simulations, and \mathbf{I}_v and $\hat{\mathbf{I}}_v$ respectively denote the v th voxel from the true parameter map and reconstructed parameter map. Note that

$$\text{NRMSE}_n = \sqrt{\text{NBias}_n^2 + \text{NVar}_n^2}.$$

Fig. 6 shows the normalized bias, variance, and root-mean-square error maps for the reconstructed T_1 and T_2 maps using different experiments. As can be seen, the normalized bias for the ML reconstruction is much smaller than its normalized variance, and thus the root-mean-square error is dominated by the normalized variance. Given that the ML reconstruction is asymptotically unbiased [13], this can be expected. Moreover, Optimized-I and Optimized-II improve the normalized variances for both T_1 and T_2 maps. Similar to the previous results, the improvement for the T_2 map is

more substantial than that for the T_1 map. Moreover, we evaluated fully-sampled MR fingerprinting experiments with different acquisition lengths, using the acquisition parameters from the conventional scheme, Optimized-I, and Optimized-II. Here we considered the acquisition lengths ranging from $N = 300$ to $N = 800$, all with $\text{SNR} = 33$ dB. Fig. 7 shows the overall reconstruction error versus the acquisition length. Clearly, the optimized acquisition schemes improve over the conventional scheme for all the acquisition lengths for both T_1 and T_2 maps, although the improvement is more significant for the T_2 map as the acquisition length becomes short. As one more example, we show the reconstruction results for the acquisition length $N = 600$ in the supplementary material.

Finally, we evaluated fully-sampled MR fingerprinting experiments with different SNR levels, using the acquisition parameters from the conventional scheme, and two optimized schemes. Here we considered the SNR level ranging from 28 dB to 38 dB, all at the acquisition length $N = 400$. Fig. 8 shows the overall reconstruction error versus the SNR. As can be seen, the optimized acquisition schemes provide better accuracy for both T_1 and T_2 maps over all the SNR levels. Here the improvement is more significant for the T_2 map, especially when the SNR becomes low.

5) *Evaluation of highly-undersampled experiments:* We evaluated the optimized acquisition parameters for highly-sampled MR fingerprinting experiments as described in Section III (a). Note that this scenario is of most interest for quantitative MRI with MR fingerprinting. Specifically, we simulated highly-undersampled experiments at $N = 400$ and $\text{SNR} = 33$ dB, using three different sets of acquisition parameters, i.e., the conventional scheme, Optimized-I, and Optimized-II. Fig. 9 shows the reconstructed T_1 and T_2 maps from the above experiments. As can be seen, compared to the conventional scheme, Optimized-I improves the accuracy of the T_2 map, but at the expense of degrading the accuracy of T_1 map. In contrast, Optimized-II provides better accuracy for both T_1 and T_2 maps, which can be highly desirable. Here note that both optimized schemes enable the substantial improvement in the accuracy of the T_2 map.

Here it is worth making some remarks on the above results. First, note that the ML reconstruction for MR fingerprinting involves solving a nonlinear and nonconvex optimization problem, for which a good initialization is often required. By enforcing the additional constraint on the flip angle variations, we are able to obtain much smoother magnetization evolutions from Optimized-II as shown in Fig. 3. Given highly-undersampled data, this often leads to better pattern matching performance with the gridding reconstruction that suffer from significant aliasing. This in turn provides a better initialization for the ML reconstruction, and leads to better performance.

We further studied the bias-variance property of the reconstructed parameter maps. Specifically, we performed Monte Carlo simulations with 100 trials. In Fig. 3, we show the normalized bias, variance, and root-mean-square error for the reconstructed T_1 and T_2 maps. As can be seen, compared to the conventional scheme, Optimized-II reduces the normalized variance and root-mean-square error for both T_1 and T_2 maps. Moreover, compared to Optimized-I, Optimized-II dramati-

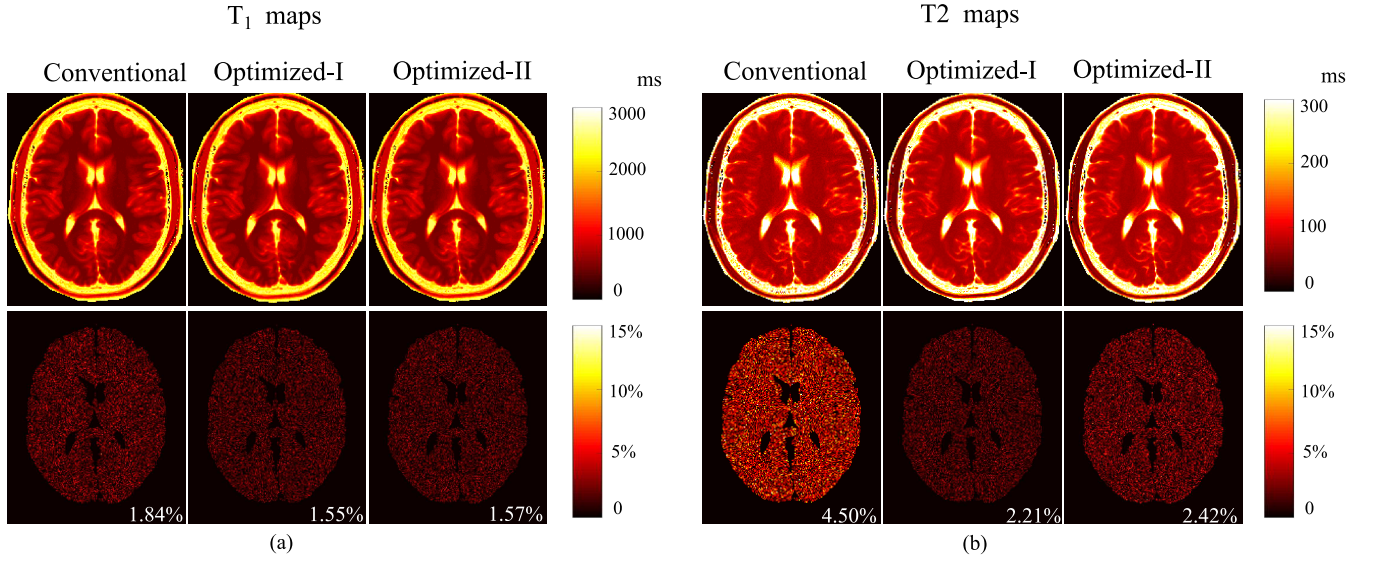


Fig. 5. Reconstructed parameter maps from the fully-sampled MR fingerprinting experiments ($N = 400$ and $\text{SNR} = 33$ dB), using the acquisition parameters from the conventional scheme, Optimized-I, and Optimized-II. (a) Reconstructed T_1 maps and associated relative error maps. (b) Reconstructed T_2 maps and associated relative error maps. Note that the overall error is labeled at the lower right corner of each error map, and the regions associated with the background, skull, scalp, and CSF were set to be zero.

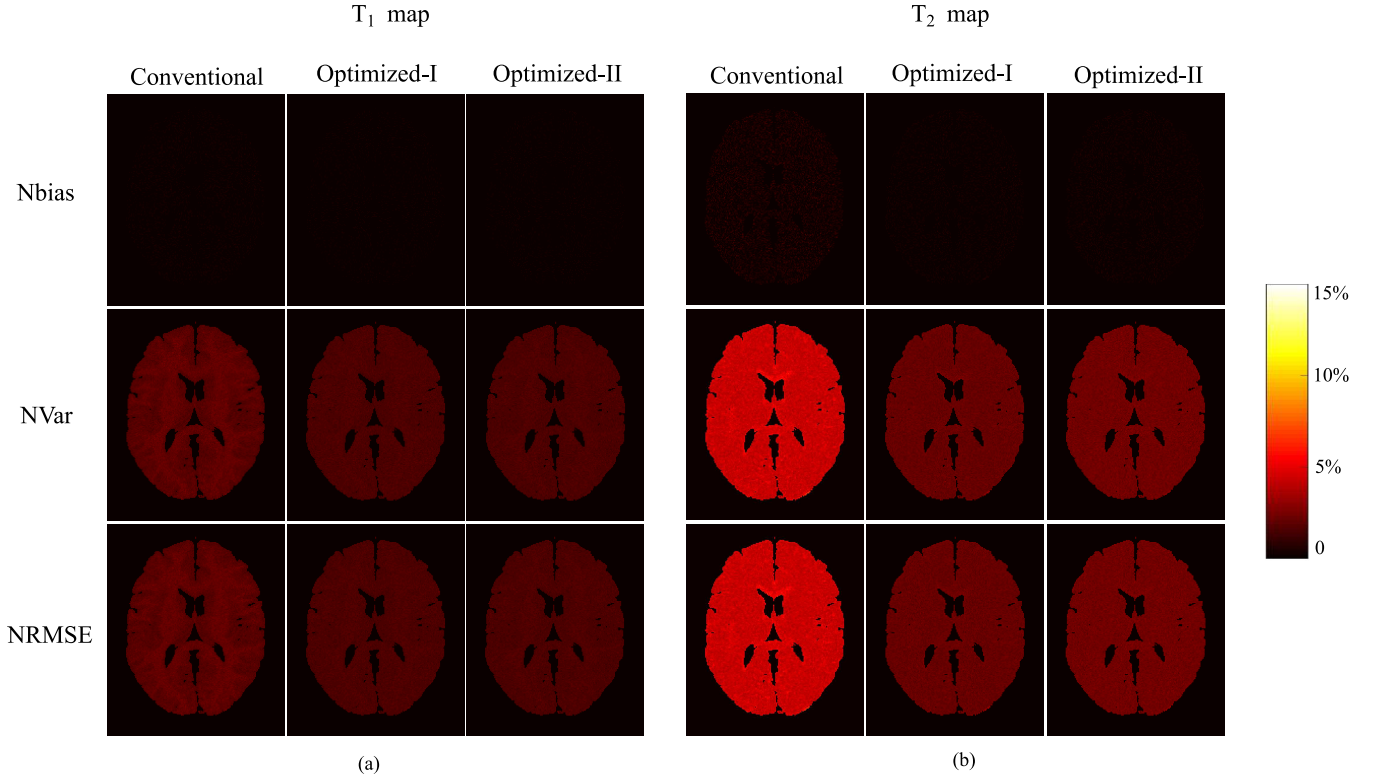
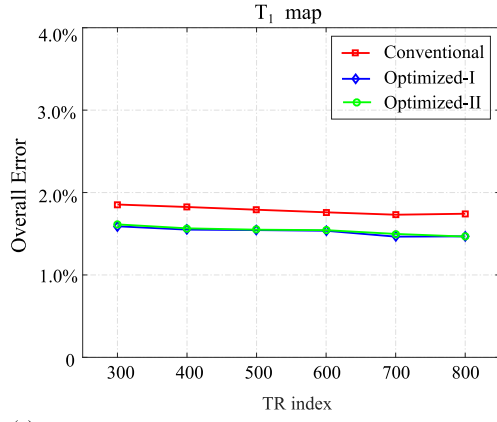


Fig. 6. Bias-variance analysis of the reconstructed parameter maps from the fully-sampled MR fingerprinting experiments ($N = 400$ and $\text{SNR} = 33$ dB), using the acquisition parameters from the conventional scheme, Optimized-I, and Optimized-II. (a) Normalized bias, variance, and root-mean-square error for (a) T_1 maps and (b) T_2 maps. The regions associated with the background, skull, scalp, and CSF were set to be zero.

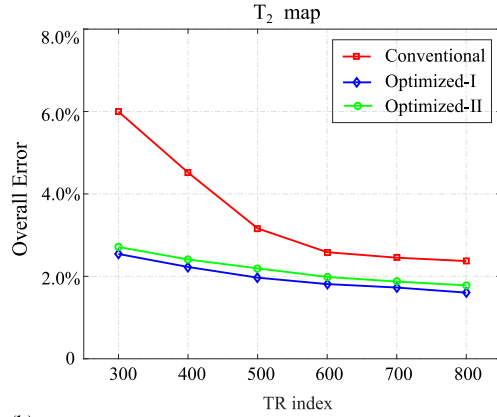
cally reduces the bias with smooth magnetization evolutions. This set of results further illustrates the merit of introducing the flip angle variation constraint into the experiment design.

In addition, we evaluated highly-undersampled MR fingerprinting experiments with different acquisition lengths, ranging from $N = 300$ to $N = 800$. Here, for each acquisition length,

we simulated the imaging experiments using the acquisition parameters from the conventional scheme, Optimized-I, and Optimized-II. We set $\text{SNR} = 33$ dB for all the experiments. Fig. 11 shows the overall error versus the acquisition length. As can be seen, Optimized-II outperforms the conventional scheme and Optimized-I for all the acquisition lengths. As



(a)



(b)

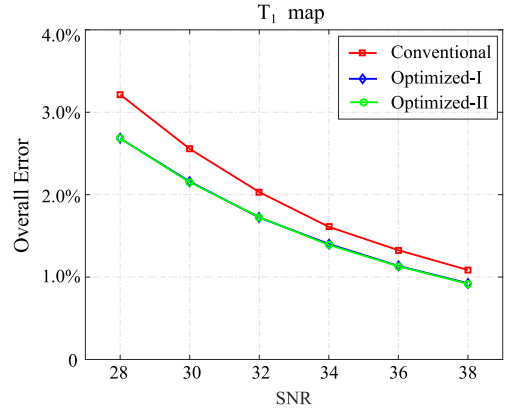
Fig. 7. Overall error versus the acquisition length for fully-sampled MR fingerprinting experiments using the acquisition parameters from the conventional scheme, and two optimized schemes. (a) Overall error for the T_1 map. (b) Overall error for the T_2 map.

a further illustration, we show the reconstruction results from the acquisition length $N = 600$ in the supplementary material.

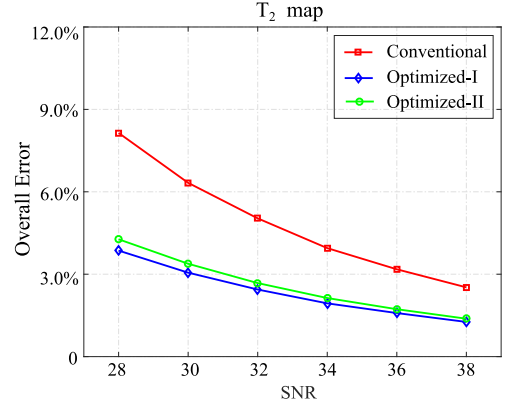
Finally, we evaluated highly-undersampled MR fingerprinting experiments at different SNR levels, ranging from 28 dB to 38 dB. For each SNR level, we simulated the imaging experiments using the acquisition parameters from the conventional scheme, Optimized-I, and Optimized-II. Here we set the acquisition length as $N = 400$ for all the experiments. Fig. 12 shows the overall error versus the SNR for the T_1 and T_2 maps. It is clear that the optimized-II provides better accuracy than the conventional scheme and Optimized-I for all the SNR levels.

B. Phantom Experiments

We performed phantom experiments to evaluate the performance of the optimized acquisition parameters. Specifically, we created a physical phantom that consists of 9 plastic tubes. We filled each tube with a solution that had Gadolinium and Agar of different concentrations, which created different combinations of T_1 and T_2 values that are relevant to the neuroimaging application [48]. We conducted the imaging experiments on a 3T Siemens Tim Trio scanner (Siemens Medical Solutions, Erlangen, Germany) equipped with a 32-



(a)



(b)

Fig. 8. Overall error versus the SNR level for fully-sampled MR fingerprinting experiments using the acquisition parameters from the conventional scheme, and two optimized schemes. (a) Overall error for the T_1 map. (b) Overall error for the T_2 map.

channel head array coil. We set the FOV = 300×300 mm², matrix size = 256×256 , and slice thickness = 5 mm for our experiments.

Here we focus on the scenario of highly-undersampled experiments, which is of most practical interest. Specifically, we performed two sets of highly-undersampled MR fingerprinting experiments with $N = 400$, respectively, using the acquisition parameters from the conventional scheme and Optimized-II.⁸ We used the same spiral trajectory and sampling pattern as in our numerical simulations. Here the acquisition times for the conventional scheme and Optimized-II were 5.28 sec and 5.22 sec, respectively. To evaluate the performance of the above experiments, we also acquired a set of reference T_1 and T_2 maps, by performing a fully-sampled MR fingerprinting experiment⁹ with $N = 1000$ using the acquisition parameters from the conventional scheme. The acquisition time for this

⁸Given that Optimized-II outperforms Optimized-I for highly-undersampled MR fingerprinting experiments, we only considered Optimized-II for our phantom experiments.

⁹Note that the fully-sampled experiment was performed by repeating a highly-undersampled MR fingerprinting experiment multiple times. For each time, we switched to a different spiral interleaves for $\{(\alpha_n, TR_n)\}$, until we collected a full set of spiral interleaves for all $\{(\alpha_n, TR_n)\}$. Here we added a short time delay between each undersampled imaging experiment, which ensures that the magnetization returns to thermal equilibrium.

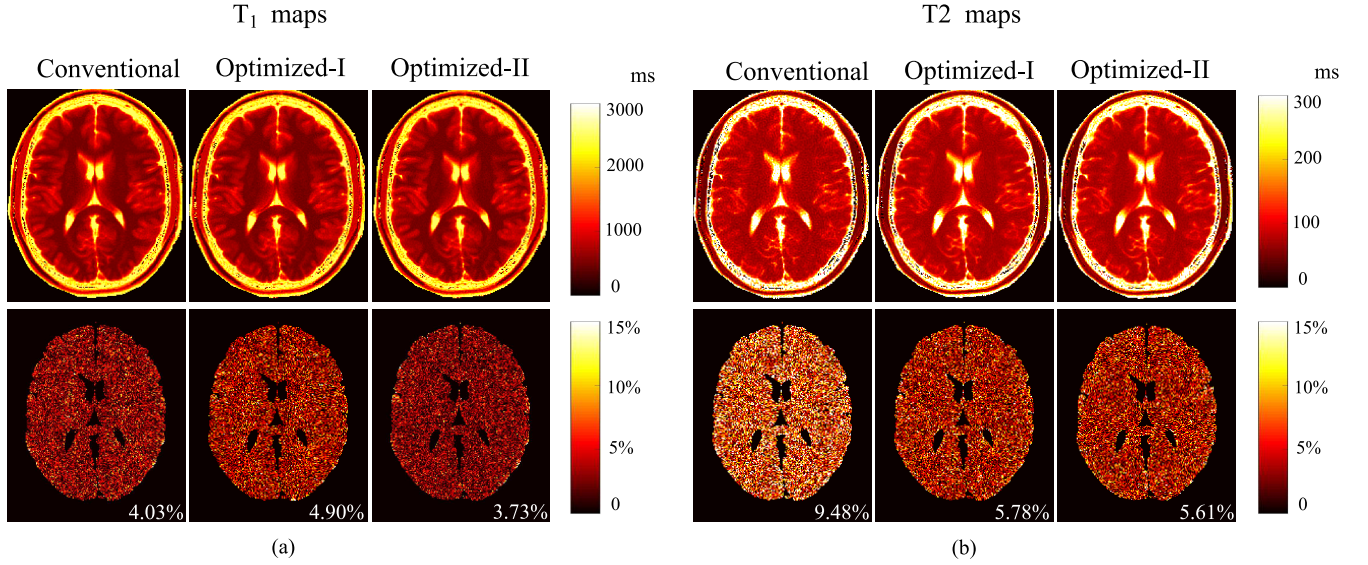


Fig. 9. Reconstructed parameter maps from the highly-undersampled MR fingerprinting experiments ($N = 400$ and $\text{SNR} = 33$ dB), using the acquisition parameters from the conventional scheme, Optimized-I, and Optimized-II. (a) Reconstructed T_1 maps and associated relative error maps. (b) Reconstructed T_2 maps and associated relative error maps. Note that the overall error is labeled at the lower right corner of each error map, and the regions associated with the background, skull, scalp, and CSF were set to be zero.

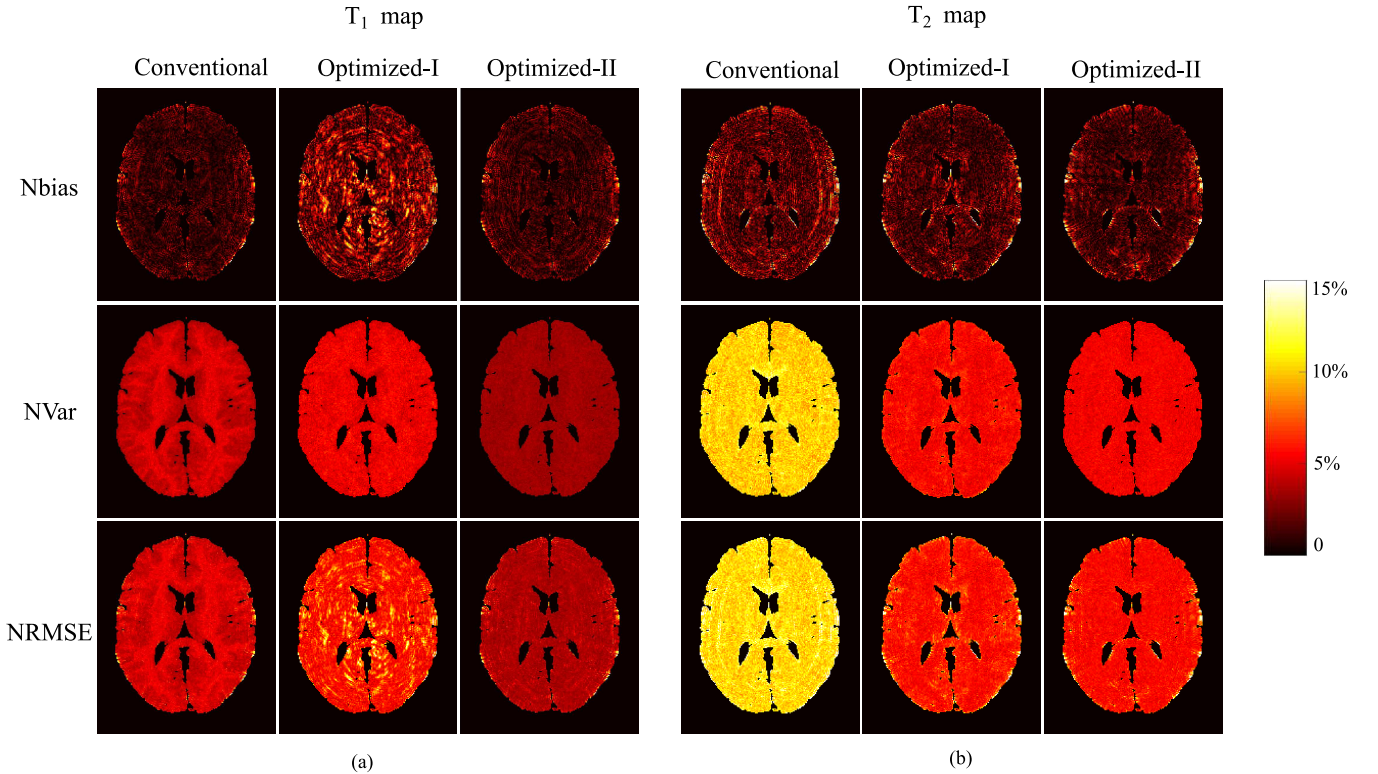
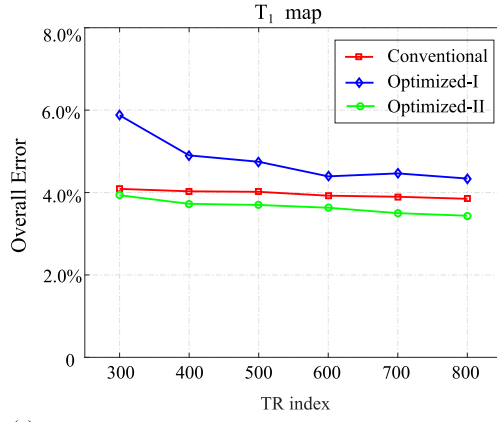


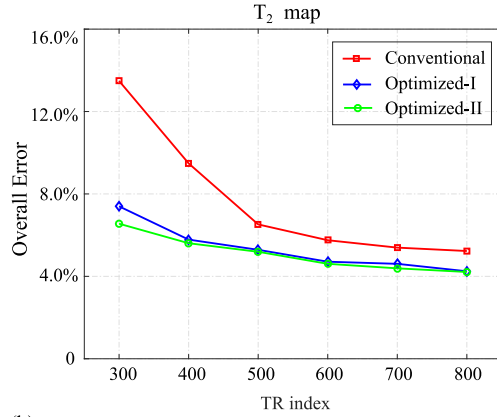
Fig. 10. Bias-variance analysis of the reconstructed parameter maps from the highly-undersampled MR fingerprinting experiments ($N = 400$ and $\text{SNR} = 33$ dB), using the acquisition parameters from the conventional scheme, Optimized-I, and Optimized-II. (a) Normalized bias, variance, and root-mean-square error for (a) T_1 maps and (b) T_2 maps. The regions associated with the background, skull, scalp, and CSF were set to be zero.

experiment was about 18 min. Besides, we also measured the actual spiral trajectory with a specialized pulse sequence, which avoids the potential trajectory distortion caused by eddy currents and gradient delay [49]. Finally, we performed a calibration scan with a gradient echo sequence, from which we estimated the coil sensitivity maps using the subspace

method [50]. We performed the ML reconstruction for the above experiments, and used the same dictionary as in our numerical simulation. Fig. 13 shows the reconstructed T_1 and T_2 maps as well as the relative error maps (evaluated with respect to the reference data). Fig. 14 shows the corresponding reconstruction errors with respect to each tube. As can be seen,



(a)



(b)

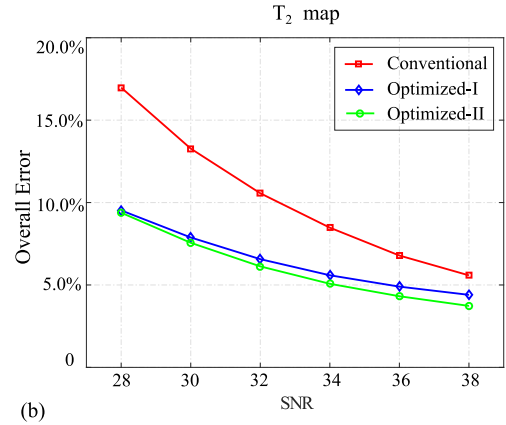
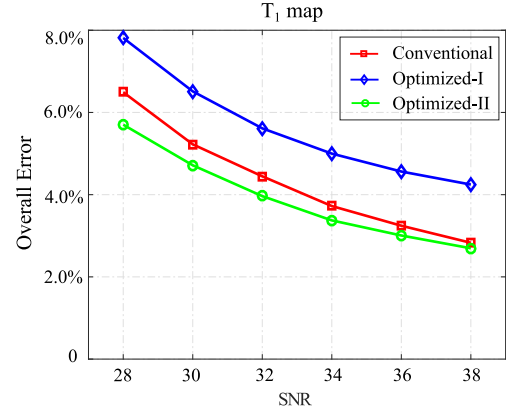
Fig. 11. Overall error versus the acquisition length for the highly-undersampled MR fingerprinting experiments using the acquisition parameters from the conventional scheme, and two optimized schemes. (a) Overall error for the T_1 map. (b) Overall error for the T_2 map. Note that the background region was set to be zero.

Optimized-II significantly improves the accuracy of the T_2 map, while providing similar accuracy for the T_1 map. This set of phantom experiments provides a further confirmation for the effectiveness of the proposed experiment design.

IV. DISCUSSION

In this work, we used the data model (8) to optimize acquisition parameters of MR fingerprinting experiments. This simplifies the computational problem. As demonstrated in Section III, it works well for highly-undersampled experiments, by incorporating the additional constraints that enforce the smoothness of magnetization evolutions. As a generalization, it would be interesting to study the problem of jointly designing acquisition parameters and k-space trajectory, although the CRB calculation in this case requires the complete data model [9], which can be computationally more expensive.

By solving the experiment design problems in (18) and (19), we observed that the optimized acquisition parameters appeared to be highly structured. In particular, the optimized repetition times appeared to be binary. This interesting behavior is worth an in-depth study. As shown in [21], [51], certain CRB based experiment design problem that involves a dynamic system can be casted as an optimal control problem.



(b)

Fig. 12. Overall error versus the SNR level for the highly-undersampled MR fingerprinting experiments using the acquisition parameters from the conventional scheme, and two optimized schemes. (a) Overall error for the T_1 map. (b) Overall error for the T_2 map.

Given such an inherent connection, our observation may be explained by the Bang-Bang control principle [22].¹⁰ Although proving this principle for the solution to (18) and (19) is beyond the scope of this paper, we plan to conduct a control-theoretic study of the problem, and will report related results in the future work. On the other hand, we could utilize the fact that (18) and (19) admit structured solutions to design more efficient algorithms to solve the experiment design problem.

Considering that the CRBs associated with (8) depend on true tissue parameters, we manually selected a few representative tissues to perform experiment design. Given a specific imaging application of interest (e.g., neuroimaging), the range of tissue parameter values, e.g., T_1 and T_2 , are often known a priori. Thus, this approach is feasible. In practice, it performs well, as demonstrated in the numerical simulations and phantom experiments. From a Bayesian perspective, this approach is equivalent to assuming that there are a finite number of tissue types, and each tissue has the equal probability. With this viewpoint, we can generalize our approach to incorporate

¹⁰To the best of our knowledge, this work is the first that reports the Bang-Bang type of behavior for the optimized acquisition parameters. Although Maidens et al. formulated the experiment design problem as an optimal control problem, and derived the approximate dynamic programming based algorithm, they only considered a highly-simplified problem setup and did not report the Bang-Bang behavior.

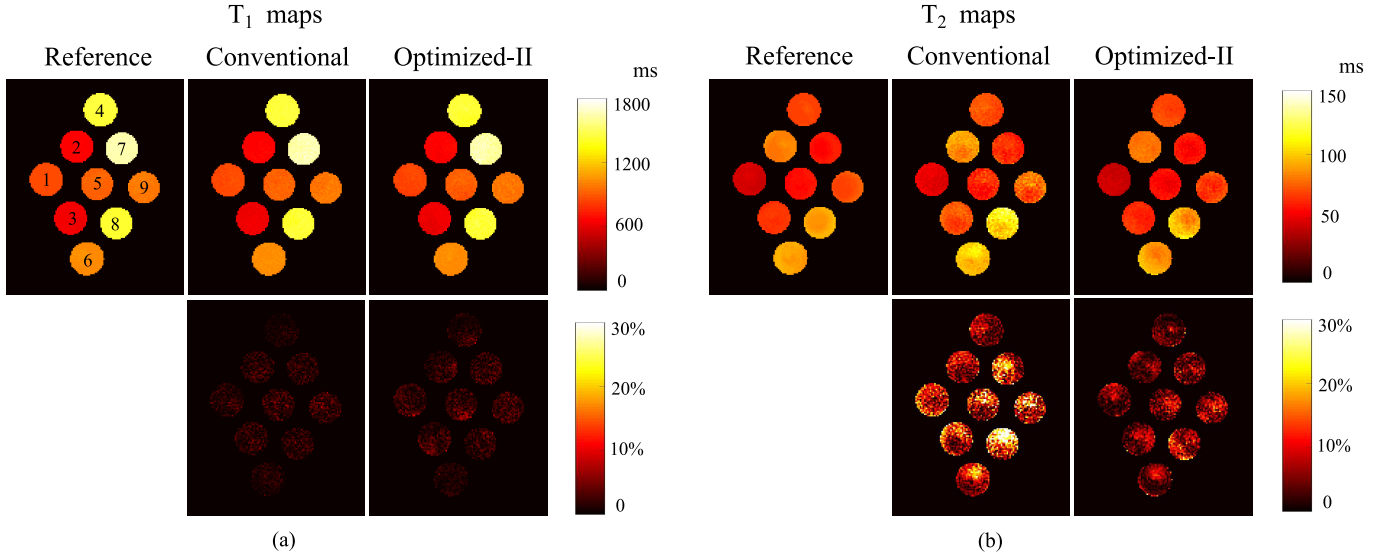


Fig. 13. Reconstructed parameter maps for the phantom experiments ($N = 400$) using the acquisition parameters from the conventional scheme, and Optimized-II. (a) Reconstructed T_1 map and associated relative error map. (b) Reconstructed T_2 map and associated relative error map. Note that the highly-undersampled MR fingerprinting experiments using the conventional scheme and optimized-II respectively took 5.28 sec and 5.22 sec, whereas the fully-sampled MR fingerprinting experiment for the reference data took 18.3 min.

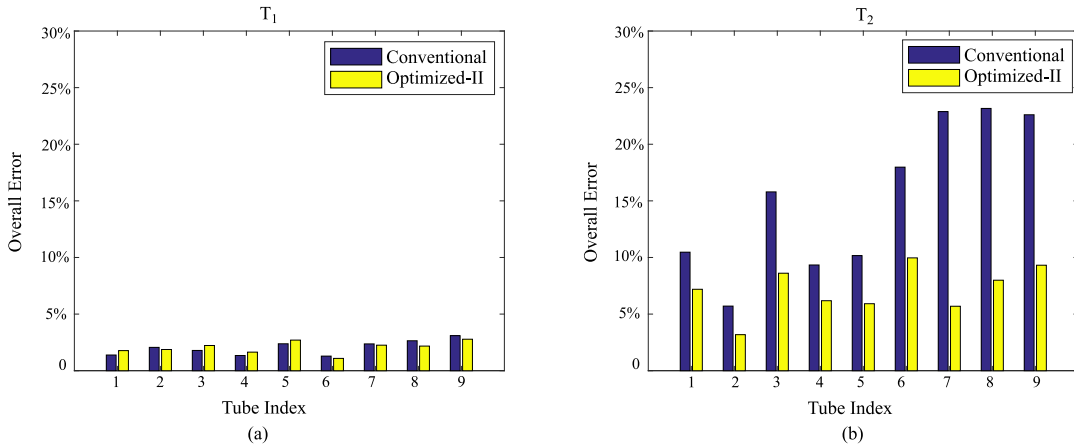


Fig. 14. Reconstruction errors for the phantom experiments ($N = 400$) using the acquisition parameters from the conventional scheme, and Optimized-II. (a) Overall error of the T_1 reconstruction at each tube. (b) Overall error of the T_2 reconstruction at each tube.

more complex probability distributions on tissues parameter values [33], and perform optimal experiment design with the Bayesian CRB [52]. Besides the Bayesian paradigm, we can also use the min-max criterion for experiment design [31], which may provide more robust performance.

We manually chose the parameters of the weighting matrix and the constraint sets for (18) and (19), which provided good performance for the neuroimaging application in this work. Note that for other different applications, we should adjust these parameters accordingly. For example, in cardiac MR fingerprinting experiments [53], we may want to constrain flip angles to be small, and apply multiple preparation RF pulses in the acquisition train.

We demonstrated the performance of the optimized MR fingerprinting experiments with both numerical simulations and phantom experiments. In the future work, it is worth evaluating the robustness of the proposed approach with in-

vivo data. But, note that for in-vivo experiments, a variety of model mismatches (e.g., tissue partial volume effect) exist, and can complicate the method evaluation and validation [31], [54]. In this case, the interpretation of results can become more subtle.

In this work, we optimized MR fingerprinting experiments with the CRB to improve the SNR efficiency. Besides the SNR consideration, there are a number of other criteria that could be used to design experiments. For example, as demonstrated in [55], one can design acquisition parameters to improve the patient comfort in an MR fingerprinting experiment. In the future work, it would be interesting to study the experiment design problem that incorporates more than one design criterion (e.g., both the SNR efficiency and patient comfort). It may be desirable to obtain a solution that can effectively trade off different design considerations.

V. CONCLUSION

In this work, we presented an estimation-theoretic framework to perform optimal experiment design for MR fingerprinting. We described a discrete-time dynamic system to model spin dynamics that underlie MR fingerprinting experiments. With this model, we calculated the Cramér-Rao bound, and formulated an optimal experiment design problem to optimize data acquisition parameters for an MR fingerprinting experiment. We demonstrated the effectiveness of the proposed approach with both simulation data and experimental data. Remarkably, we found that the optimized acquisition parameters appear to be highly structured, rather than random/pseudo-randomly varying as used in the existing MR fingerprinting experiments.

VI. APPENDIX

In this appendix, we derive the Jacobian matrix $\mathbf{J}_n(\boldsymbol{\theta})$ in (14) for the IR-FISP sequence. This serves as an example to illustrate the procedure described in (15) and (16). Recall that in the IR-FISP sequence, $\boldsymbol{\theta} = [T_1, T_2, M_0]^T$ and

$$\mathbf{J}_n(\boldsymbol{\theta}) = \frac{\partial \mathbf{m}[n]}{\partial \boldsymbol{\theta}} = \begin{bmatrix} \frac{\partial}{\partial T_1} \mathbf{m}[n] & \frac{\partial}{\partial T_2} \mathbf{m}[n] & \frac{\partial}{\partial M_0} \mathbf{m}[n] \end{bmatrix}.$$

For clarity, we first summarize the state-space model for the IR-FISP sequence as follows:

$$\mathbf{M}_r[n] = \mathbf{G}(\beta_r) \mathbf{R}(T_1, T_2, TR_n) \mathbf{Q}(\alpha_n, \phi_n) \mathbf{M}_r[n-1] + \frac{M_0}{N_v} \mathbf{b}(T_1, TR_n), \quad (20)$$

$$\mathbf{m}[n] = \sum_r \mathbf{P} \mathbf{R}(T_1, T_2, TE_n) \mathbf{Q}(\alpha_n, \phi_n) \mathbf{M}_r[n-1], \quad (21)$$

for $n = 1, \dots, N$. Next, we calculate the derivatives of $\mathbf{m}[n]$ with respect to T_1 , T_2 , and M_0 based on (15) and (16).

A. Derivative of \mathbf{m}^n with respect to T_1

Invoking the derivative with respect to T_1 on both sides of (21), we have

$$\frac{\partial \mathbf{m}[n]}{\partial T_1} = \sum_r \left\{ \mathbf{P} \frac{\partial \mathbf{R}(T_1, T_2, TE_n)}{\partial T_1} \mathbf{Q}(\alpha_n, \phi_n) \mathbf{M}_r[n-1] + \mathbf{P} \mathbf{R}(T_1, T_2, TE_n) \mathbf{Q}(\alpha_n, \phi_n) \frac{\partial \mathbf{M}_r[n-1]}{\partial T_1} \right\}, \quad (22)$$

where

$$\frac{\partial \mathbf{R}(T_1, T_2, TE_n)}{\partial T_1} = \frac{TE_n}{T_1^2} \exp\left(-\frac{TE_n}{T_1}\right) \begin{bmatrix} 0 & 0 & 0 \\ 0 & 0 & 0 \\ 0 & 0 & 1 \end{bmatrix}.$$

Noting that

$$\mathbf{P} \frac{\partial \mathbf{R}(T_1, T_2, TE_n)}{\partial T_1} = \mathbf{0},$$

(22) can be simplified as

$$\frac{\partial \mathbf{m}[n]}{\partial T_1} = \sum_r \mathbf{P} \mathbf{R}(T_1, T_2, TE_n) \mathbf{Q}(\alpha_n, \phi_n) \frac{\partial \mathbf{M}_r[n-1]}{\partial T_1}. \quad (23)$$

We then take the derivative with respect to T_1 on both sides of (20), i.e.,

$$\begin{aligned} \frac{\partial \mathbf{M}_r[n]}{\partial T_1} &= \mathbf{G}(\beta_r) \frac{\partial \mathbf{R}(T_1, T_2, TR_n)}{\partial T_1} \mathbf{Q}(\alpha_n, \phi_n) \mathbf{M}_r[n-1] \\ &+ \mathbf{G}(\beta_r) \mathbf{R}(T_1, T_2, TR_n) \mathbf{Q}(\alpha_n, \phi_n) \frac{\partial \mathbf{M}_r[n-1]}{\partial T_1} \\ &+ \frac{M_0}{N_v} \frac{\partial b(T_1, TR_n)}{\partial T_1}, \end{aligned} \quad (24)$$

where

$$\frac{\partial \mathbf{R}(T_1, T_2, TR_n)}{\partial T_1} = \frac{TR_n}{T_1^2} \exp\left(-\frac{TR_n}{T_1}\right) \begin{bmatrix} 0 & 0 & 0 \\ 0 & 0 & 0 \\ 0 & 0 & 1 \end{bmatrix},$$

and

$$\frac{\partial b(T_1, TR_n)}{\partial T_1} = -\frac{TR_n}{T_1^2} \exp\left(-\frac{TR_n}{T_1}\right).$$

Here we can calculate $\partial \mathbf{m}[n]/\partial T_1$ by iterating (23) and (24) with the initial conditions $\mathbf{M}_r[0] = \frac{M_0}{N_v} [0 \ 0 \ 1]^T$ and $\partial \mathbf{M}_r[0]/\partial T_1 = [0 \ 0 \ 0]^T$.

B. Derivative of \mathbf{m}^n with respect to T_2

Invoking the derivative respect to T_2 on both sides of (21), we have

$$\begin{aligned} \frac{\partial \mathbf{m}[n]}{\partial T_2} &= \sum_r \left\{ \mathbf{P} \frac{\partial \mathbf{R}(T_1, T_2, TE_n)}{\partial T_2} \mathbf{Q}(\alpha_n, \phi_n) \mathbf{M}_r[n-1] \right. \\ &\left. + \mathbf{P} \mathbf{R}(T_1, T_2, TE_n) \mathbf{Q}(\alpha_n, \phi_n) \frac{\partial \mathbf{M}_r[n-1]}{\partial T_2} \right\}, \end{aligned} \quad (25)$$

where

$$\frac{\partial \mathbf{R}(T_1, T_2, TE_n)}{\partial T_2} = \frac{TE_n}{T_2^2} \exp\left(-\frac{TE_n}{T_2}\right) \begin{bmatrix} 1 & 0 & 0 \\ 0 & 1 & 0 \\ 0 & 0 & 0 \end{bmatrix}.$$

We then take the derivative with respect to T_2 on both sides of (20), i.e.,

$$\begin{aligned} \frac{\partial \mathbf{M}_r[n]}{\partial T_2} &= \mathbf{G}(\beta_r) \frac{\partial \mathbf{R}(T_1, T_2, TR_n)}{\partial T_2} \mathbf{Q}(\alpha_n, \phi_n) \mathbf{M}_r[n-1] \\ &+ \mathbf{G}(\beta_r) \mathbf{R}(T_1, T_2, TR_n) \mathbf{Q}(\alpha_n, \phi_n) \frac{\partial \mathbf{M}_r[n-1]}{\partial T_2}, \end{aligned} \quad (26)$$

where

$$\frac{\partial \mathbf{R}(T_1, T_2, TR_n)}{\partial T_2} = \frac{TR_n}{T_2^2} \exp\left(-\frac{TR_n}{T_2}\right) \begin{bmatrix} 1 & 0 & 0 \\ 0 & 1 & 0 \\ 0 & 0 & 0 \end{bmatrix}.$$

Here we can calculate $\partial \mathbf{m}[n]/\partial T_2$ by iterating (25) and (26) with the initial conditions $\mathbf{M}_r[0] = \frac{M_0}{N_v} [0 \ 0 \ 1]^T$ and $\partial \mathbf{M}_r[0]/\partial T_2 = [0 \ 0 \ 0]^T$.

C. Derivative of \mathbf{m}^n with respect to M_0

Invoking the derivative with respect to M_0 on both sides of (21), we have

$$\frac{\partial \mathbf{m}[n]}{\partial M_0} = \sum_{\mathbf{r}} \mathbf{PR}(T_1, T_2, TE_n) \mathbf{Q}(\alpha_n, \phi_n) \frac{\partial \mathbf{M}_{\mathbf{r}}[n-1]}{\partial M_0}. \quad (27)$$

We then take the derivative with respect to M_0 on both sides of (20), i.e.,

$$\begin{aligned} \frac{\partial \mathbf{M}[n]}{\partial M_0} &= \mathbf{G}(\beta_{\mathbf{r}}) \mathbf{R}(T_1, T_2, TR_n) \mathbf{Q}(\alpha_n, \phi_n) \frac{\partial \mathbf{M}_{\mathbf{r}}[n-1]}{\partial M_0} \\ &\quad + \frac{1}{N_v} b(T_1, TR_n). \end{aligned} \quad (28)$$

Here we can calculate $\partial \mathbf{m}[n]/\partial M_0$ by iterating (27) and (28) with the initial condition $\partial \mathbf{M}_{\mathbf{r}}[0]/\partial M_0 = \frac{1}{N_v} [0 \ 0 \ 1]^T$.

REFERENCES

- [1] D. Ma, V. Gulani, N. Seiberlich, K. Liu, J. L. Sunshine, J. L. Duerk, and M. A. Griswold, "Magnetic resonance fingerprinting," *Nature*, vol. 495, pp. 187–192, 2013.
- [2] K. Scheffler and J. Hennig, "T1 quantification with inversion recovery TrueFISP," *Magn. Reson. Med.*, vol. 45, pp. 720–723, 2001.
- [3] S. C. Deoni, B. K. Rutt, and T. M. Peters, "Rapid combined T1 and T2 mapping using gradient recalled acquisition in the steady state," *Magn. Reson. Med.*, vol. 49, no. 3, pp. 515–526, 2003.
- [4] P. Schmitt, M. A. Griswold, P. M. Jakob, M. Kotas, V. Gulani, M. Flentje, and A. Haase, "Inversion recovery TrueFISP: Quantification of T1, T2, and spin density," *Magn. Reson. Med.*, vol. 51, no. 4, pp. 661–667, 2004.
- [5] J. Warntjes, O. Dahlqvist, and P. Lundberg, "Novel method for rapid, simultaneous T1, T2*, and proton density quantification," *Magn. Reson. Med.*, vol. 57, no. 3, pp. 528–537, 2007.
- [6] P. Ehses, N. Seiberlich, D. Ma, F. A. Breuer, P. M. Jakob, M. A. Griswold, and V. Gulani, "IR TrueFISP with a golden-ratio-based radial readout: Fast quantification of T1, T2, and proton density," *Magn. Reson. Med.*, vol. 69, pp. 71–81, 2013.
- [7] M. Davies, G. Puy, P. Vandergheynst, and Y. Wiaux, "A compressed sensing framework for magnetic resonance fingerprinting," *SIAM J. Imaging Sciences*, vol. 7, pp. 2623–2656, 2014.
- [8] B. Zhao, F. Lam, B. Bilgic, H. Ye, and K. Setsompop, "Maximum likelihood reconstruction for magnetic resonance fingerprinting," in *Proc. IEEE Int. Symp. Biomed. Imaging*, 2015, pp. 905–909.
- [9] B. Zhao, K. Setsompop, H. Ye, S. Cauley, and L. L. Wald, "Maximum likelihood reconstruction for magnetic resonance fingerprinting," *IEEE Trans. Med. Imaging*, vol. 35, pp. 1812–1823, 2016.
- [10] E. Y. Pierre, D. Ma, Y. Chen, C. Badve, and M. A. Griswold, "Multiscale reconstruction for MR fingerprinting," *Magn. Reson. Med.*, vol. 75, no. 6, pp. 2481–2492, 2016.
- [11] X. Cao, C. Liao, Z. Wang, Y. Chen, H. Ye, H. He, and J. Zhong, "Robust sliding-window reconstruction for accelerating the acquisition of MR fingerprinting," *Magn. Reson. Med.*, vol. 78, pp. 1579–1588, 2017.
- [12] B. Zhao, K. Setsompop, E. Adalsteinsson, B. Gagoski, H. Ye, D. Ma, Y. Jiang, P. E. Grant, M. A. Griswold, and L. L. Wald, "Improved magnetic resonance fingerprinting reconstruction with low-rank and subspace modeling," *Magn. Reson. Med.*, 2017, in press.
- [13] S. M. Kay, *Fundamentals of Statistical Signal Processing: Estimation Theory*. Upper Saddle River, NJ: Prentice Hall, 1993, vol. I.
- [14] Y. Jiang, D. Ma, N. Seiberlich, V. Gulani, and M. A. Griswold, "MR fingerprinting using fast imaging with steady state precession (FISP) with spiral readout," *Magn. Reson. Med.*, vol. 74, no. 6, pp. 1621–1631, 2015.
- [15] J. Assländer, S. J. Glaser, and J. Hennig, "Pseudo steady-state free precession for MR-fingerprinting," *Magn. Reson. Med.*, vol. 77, no. 3, pp. 1151–1161, 2017.
- [16] Y. Jiang, D. Ma, R. Jeremic, J. Duerk, N. Seiberlich, V. Gulani, and M. A. Griswold, "MR fingerprinting using the quick echo splitting NMR imaging technique," *Magn. Reson. Med.*, vol. 77, no. 3, pp. 979–988, 2017.
- [17] B. Rieger, F. Zimmer, J. Zapp, S. Weingärtner, and L. R. Schad, "Magnetic resonance fingerprinting using echo-planar imaging: Joint quantification of T1 and T2* relaxation times," *Magn. Reson. Med.*, in press.
- [18] B. Zhao, J. P. Haldar, K. Setsompop, and L. L. Wald, "Towards optimized experiment design for magnetic resonance fingerprinting," in *Proc. Int. Symp. Magn. Reson. Med.*, 2016, p. 2835.
- [19] —, "Optimal experiment design for magnetic resonance fingerprinting," in *Proc. IEEE Eng. Med. Bio. Conf.*, 2016, pp. 453–456.
- [20] J. Assländer, D. Sodickson, R. Lattanzi, and M. Cloos, "Relaxation in Polar Coordinates: Analysis and Optimization of MR-Fingerprinting," in *Proc. Int. Symp. Magn. Reson. Med.*, 2017, p. 127.
- [21] J. Maidens, A. Packard, and A. M., "Parallel dynamic programming for optimal experiment design in nonlinear systems," in *55th IEEE Conf. on Decision and Control*, 2016, pp. 2894–2899.
- [22] D. P. Bertsekas, *Dynamic Programming and Optimal Control*. Belmont, MA: Athena Scientific, 2017, vol. I.
- [23] O. Cohen and M. S. Rosen, "Algorithm comparison for schedule optimization in MR fingerprinting," *Magn. Reson. Imaging*, in press.
- [24] J. A. Jones, P. Hodgkinson, A. L. Barker, and P. J. Hore, "Optimal sampling strategies for the measurement of spin-spin relaxation times," *J. Magn. Reson. Ser B*, vol. 113, pp. 25–34, 1996.
- [25] Y. Zhang, H. N. Yeung, M. O'Donnell, and P. L. Carson, "Determination of sample time for T1 measurement," *J. Magn. Reson. Imaging*, vol. 8, pp. 675–681, 1998.
- [26] J. P. Haldar, D. Hernando, and Z.-P. Liang, "Super-resolution reconstruction of MR image sequences with contrast modeling," in *Proc. IEEE Int. Symp. Biomed. Imaging*, 2009, pp. 266–269.
- [27] A. Funai and J. A. Fessler, "Cramér Rao bound analysis of joint B1/T1 mapping methods in MRI," in *Proc. IEEE Int. Symp. Biomed. Imaging*, 2010, pp. 712–715.
- [28] K. Li, Z. Zu, J. Xu, V. A. Janve, J. C. Gore, M. D. Does, and D. F. Gochberg, "Optimized inversion recovery sequences for quantitative T1 and magnetization transfer imaging," *Magn. Reson. Med.*, vol. 64, pp. 491–500, 2010.
- [29] B. Zhao, F. Lam, and Z.-P. Liang, "Model-based MR parameter mapping with sparsity constraints: Parameter estimation and performance bounds," *IEEE Trans. Med. Imaging*, vol. 33, no. 9, pp. 1832–1844, 2014.
- [30] M. Akçakaya, S. Weingärtner, S. Roujol, and R. Nezafat, "On the selection of sampling points for myocardial T1 mapping," *Magn. Reson. Med.*, vol. 73, pp. 1741–1753, 2015.
- [31] G. Nataraj, J. F. Nielsen, and J. A. Fessler, "Optimizing MR scan design for model-based T1, T2 estimation from steady-state sequences," *IEEE Trans. Med. Imaging*, vol. 36, no. 2, pp. 467–477, 2017.
- [32] R. P. A. Teixeira, S. J. Malik, and J. V. Hajnal, "Joint system relaxometry (JSR) and Cramér-Rao lower bound optimization of sequence parameters: A framework for enhanced precision of DESPOT T1 and T2 estimation," *Magn. Reson. Med.*, 2017, in press.
- [33] C. M. Lewis, S. A. Hurley, M. E. Meyerand, and C. G. Koay, "Data-driven optimized flip angle selection for T1 estimation from spoiled gradient echo acquisitions," *Magn. Reson. Med.*, vol. 76, pp. 792–802, 2016.
- [34] F. Bloch, "Nuclear induction," *Phys. Rev.*, vol. 70, pp. 460–474, 1946.
- [35] P. Shkarin and R. G. Spencer, "Time domain simulation of Fourier imaging by summation of isochromats," *Int. J. Imag. Syst. Tech.*, vol. 8, pp. 419–426, 1997.
- [36] S. J. Malik, A. Sbrizzi, H. Hoogduin, and J. V. Hajnal, "Equivalence of EPG and isochromat-based simulation of MR signals," in *Proc. Int. Symp. Magn. Reson. Med.*, 2016, p. 3196.
- [37] Z.-P. Liang and P. C. Lauterbur, *Principles of Magnetic Resonance Imaging: A Signal Processing Perspective*. New York: IEEE Press/Wiley, 1999.
- [38] F. Pukelsheim, *Optimal Design of Experiments*. New York: John Wiley and Sons, 1993.
- [39] B. Zhao, "Model-based iterative reconstruction for magnetic resonance fingerprinting," in *Proc. IEEE Int. Conf. Image Process.*, 2015, pp. 3392–3396.
- [40] J. Nocedal and S. J. Wright, *Numerical Optimization*. NY: Springer, 2006.
- [41] J. C. Spall, *Introduction to Stochastic Search and Optimization: Estimation, Simulation, and Control*. NY: John Wiley and Sons, 2003.
- [42] D. L. Collins, A. P. Zijdenbos, V. Kollokian, J. G. Sled, N. J. Kabani, C. J. Holmes, and A. C. Evans, "Design and construction of a realistic digital brain phantom," *IEEE Trans. Med. Imaging*, vol. 17, no. 3, pp. 463–468, 1998.

- [43] J. Hennig, "Multiecho imaging sequences with low refocusing flip angles," *J. Magn. Reson.*, vol. 78, pp. 397 – 407, 1988.
- [44] M. Weigel, "Extended phase graphs: Dephasing, RF pulses, and echoes - pure and simple," *J. Magn. Reson. Imaging*, vol. 41, pp. 266–295, 2015.
- [45] J. A. Fessler and B. P. Sutton, "Nonuniform fast Fourier transforms using min-max interpolation," *IEEE Trans. Signal Process.*, vol. 51, no. 2, pp. 560–574, 2003.
- [46] Y. Gao, Y. Chen, D. Ma, Y. Jiang, K. A. Herrmann, J. A. Vincent, K. M. Dell, M. L. Drumm, S. M. Brady-Kalnay, M. A. Griswold, C. A. Flask, and L. Lu, "Preclinical MR fingerprinting (MRF) at 7 T: Effective quantitative imaging for rodent disease models," *NMR Biomed.*, vol. 28, pp. 384–394, 2015.
- [47] J. P. Haldar, J. Anderson, and S. W. Sun, "Maximum likelihood estimation of T_1 relaxation parameters using VARPRO," in *Proc. Int. Symp. Magn. Reson. Med.*, 2007, p. 41.
- [48] K. Hattori, Y. Ikemoto, W. Takao, S. Ohno, T. Harimoto, S. Kanazawa, M. Oita, K. Shibuya, M. Kuroda, and H. Kato, "Development of MRI phantom equivalent to human tissues for 3.0-T MRI," *Med. Phys.*, vol. 40, p. 032303, 2013.
- [49] H. Tan and C. H. Meyer, "Estimation of k-space trajectories in spiral MRI," *Magn. Reson. Med.*, vol. 61, pp. 1396–1404, 2009.
- [50] M. Uecker, P. Lai, M. J. Murphy, P. Virtue, M. Elad, J. M. Pauly, S. S. Vasanawala, and M. Lustig, "ESPIRiT-an eigenvalue approach to autocalibrating parallel MRI: Where SENSE meets GRAPPA," *Magn. Reson. Med.*, vol. 71, pp. 990–1001, 2014.
- [51] R. T. N. Chen, "Input design for aircraft parameter identification: Using time-optimal control formulation," in *Methods for Aircraft State and Parameter Identification, Advisory Group for Aerospace Research and Development (AGARD), Conference Proceedings*, no. 172, 1975.
- [52] H. L. Van Trees and K. L. Bell, *Bayesian Bounds for Parameter Estimation and Nonlinear Filtering/Tracking*. New York: Wiley-IEEE Press, 2007.
- [53] J. I. Hamilton, A. Deshmene, S. Hougen, M. Griswold, and N. Seiberlich, "Magnetic resonance fingerprinting with chemical exchange (MRF-X) for quantification of subvoxel T_1 , T_2 , volume fraction, and exchange rate," in *Proc. Int. Symp. Magn. Reson. Med.*, 2015, p. 239.
- [54] N. Stikov, M. Boudreau, I. R. Levesque, C. L. Tardif, J. K. Barral, and G. B. Pike, "On the accuracy of T_1 mapping: Searching for common ground," *Magn. Reson. Med.*, vol. 73, pp. 514–522, 2015.
- [55] D. Ma, E. Y. Pierre, Y. Jiang, M. D. Schluchter, K. Setsompop, V. Gulani, and M. A. Griswold, "Music-based magnetic resonance fingerprinting to improve patient comfort during MRI examinations," *Magn. Reson. Med.*, vol. 75, pp. 2303–2314, 2016.